An *Ab-Initio* Study of Superconductivity in $LiAlB_4$: an MgB_2-related Compound

Mohammed Kareem Hussain

MSc by Research

University of York
Physics, Engineering, and Technology
February 2024

Abstract

Superconductors have grown in importance within materials science, largely due to their applications in magnets. Despite this, the theoretical frameworks to describe most types of superconductor remain to be understood, with a key exception in BCS-type superconductors, governed by electron-phonon interactions. Here we conduct a first principles study of the BCS-type superconductor with the highest critical temperature (T_c) at ambient pressure at around 39 K, MgB_2. In particular, we focus on crucial aspects of MgB_2 which contribute to this T_c, including the importance of the E_{2g} phonon mode involving in-plane vibrations of boron atoms. Through CASTEP, an analysis of the density of states at the Fermi energy is conducted, followed by a study of the vibrational properties of the material. Finally, the Eliashberg spectral function is used in tandem with the Allen-Dynes equation to calculate the T_c, demonstrated to be in good agreement with experimental studies at 39.16 K using $\mu^* = 0.1$. This thesis continues by introducing a new material, $LiAlB_4$, chosen from a set of metal aluminium tetraborates and containing a similar layered structure to MgB_2 with honeycomb-structured boron sheets. We find the structure to be both thermodynamically and dynamically stable, with a similar density of states at the Fermi energy as MgB_2. Also displaying similar in-plane boron vibrations, $LiAlB_4$ improves on the electron-phonon coupling strength of MgB_2 to give $T_c = 49.36$ K at ambient pressure for $\mu^* = 0.1$. This is shown to largely be the result of lower frequency phonon modes related to Li vibrations, which give stronger electron-phonon coupling.

Declaration

I declare that this thesis is a presentation of original work and I am the sole author. This work has not previously been presented for a degree or other qualification at this University or elsewhere. All sources are acknowledged as references.

Acknowledgements

First and foremost, I'd like to thank my supervisors Matt Probert and Peter Byrne, without whom this research project would not have been possible. Their support, knowledge, and kindness have been encouraging and informative through the year. I would also like to thank the rest of the York condensed matter group, who have welcomed me and provided helpful advice. In particular, Scott Donaldson has been an excellent source of conversation and provided great work with genetic algorithms to support my work in this thesis. Phil Hasnip has been a friendly face to check in on my progress during any visit to York. I'd also like to thank Andrew Higginbotham, who encouraged me with my progress in the thesis advisory panels and assisted in guiding the project's focus.

Outside of work, I'd like to thank Christopher Coveney, a lifelong friend and an exceptional scientist. He has provided both encouragement and inspiration for beginning this project, sharing a passion for science since our school years. I wish him great success in his already successful doctoral studies in Oxford. My friend Usman has been a constant source of support throughout this year, without whom life would have been much more dull. I would like to thank all my friends who have supported me throughout this year with work and with the inundations of life. Finally, I'd like to thank my partner, Pip, who has given me the confidence to pursue my project to my best capabilities and whose faith in me and intrigue in my work gave greater purpose to this year.

I dedicate this to my friend Conrad, who has shaped my life.

Contents

List of Figures

List of Tables

Chapter 1

Introduction

"In the light of the tremendous progress that has been made in raising the transition temperature of the copper oxide superconductors, it is natural to wonder how high the transition temperature, Tc, can be pushed in other classes of materials."[1]

– Jun Nagamatsu, 2001.

1.1 Superconductivity

Superconducting materials have grown in importance through the modern age, now crucial to technologies such as MRIs, fusion tokamaks, particle accelerators, and the developing maglev trains.[2] They were discovered in 1911 by Heike Kamerlingh Onnes when, upon cooling mercury to 4.2 K, he found that the electrical resistivity dropped rapidly to zero. Superconducting materials were later distinguished from perfect conductors by Walther Meissner and Robert Ochsenfeld. In 1934, they found that a superconducting material expels magnetic fields from its interior – a phenomenon since labelled as the Meissner effect. In contrast, a perfect conductor can have any constant internal field. As such, a superconductor is defined by two key properties – zero electrical resistivity and perfect diamagnetism. Over 100 years of scientific progress and intrigue has led to the discovery of hundreds of superconducting materials, each of which has a characteristic temperature at and below which superconductivity is achieved, denoted by T_c, the critical temperature. However, a material which becomes superconducting near to room temperatures remains elusive.

A breakthrough in the understanding of superconductivity was made by Bardeen, Cooper, and Schrieffer [3] in what would be described as the BCS theory of super-

conductivity. The theory predicts that below a critical temperature (T_c) a material may undergo a phase transition characterised by the formation of a large number of Cooper pairs, bound pairs of electrons. Cooper pairs form due to indirect electron-electron attractive interactions mediated by electron-phonon interactions. An electron in the crystal lattice will distort the cations around it, drawing them in to bring about a region of greater positive charge density. A distant second electron is consequentially attracted to this distortion, or phonon, thereby creating a bound pair of electrons behaving as a boson. Cooper pairs are more stable than a single electron within a lattice, able to resist thermal vibrations below the T_c. These Cooper pairs condense, much like a Bose-Einstein condensate, into a collective ground state, forming a characteristic energy gap around the Fermi level between the Cooper pair states and the normal states above. Following Cohen,[4] we can describe the relationship between the energy gap and phonons. The energy gap is related to the T_c by

$$\Delta = 1.76 k_B T_c. \tag{1.1}$$

The Debye frequency, ω_D, which describes the high-frequency cut-off for phonons in a material, is also related to the energy gap by

$$\Delta = 2\hbar\omega_D e^{-\frac{1}{N(E_f)}V}, \tag{1.2}$$

where $N(E_f)$ is the density of states at the Fermi energy (E_f) and V represents the electron-phonon attractive interaction. We can find the T_c through the Debye frequency with

$$k_B T_c = 1.13 E_D e^{-\frac{1}{\lambda-\mu}} \tag{1.3}$$

where

$$\lambda = N(E_f)V^{ph} \tag{1.4}$$

$$\mu = N(E_f)V^{C} \tag{1.5}$$

and $N(E_f)$ is the density of states at the Fermi energy and E_D is the Debye energy. λ provides an indication of the overall electron-phonon coupling strength, while μ denotes Coulombic contributions, with V^{ph} and V^C representing the phonon and Coulomb interactions respectively. As such, BCS theory imposes a limit on the critical temperature, based on reasonable assumptions of electron-phonon coupling strengths, with initial predictions of a 30 K limit.

1.2 Superconducting Magnesium Diboride

In 2001, following decades of research into the discovery of superconductors in search of higher critical temperatures, magnesium diboride was proven to be a superconductor, with a critical temperature of approximately 39 K.[1] While this was not the highest known T_c even at the time, it succeeded its intermetallic predecessors by a significant leap from around 23 K.[5] The fact that this T_c was achievable at ambient pressures with abundant constituent elements added to the excitement surrounding the discovery. The mechanism for superconductivity could be well understood within the BCS framework, yet the T_c achieved broke the expected limit due to unexpectedly strong electron-phonon coupling.

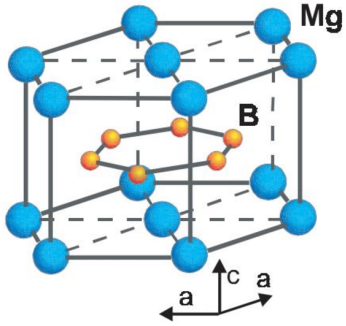

(a) The hexagonal structure of MgB_2 by Ghosh.[6]

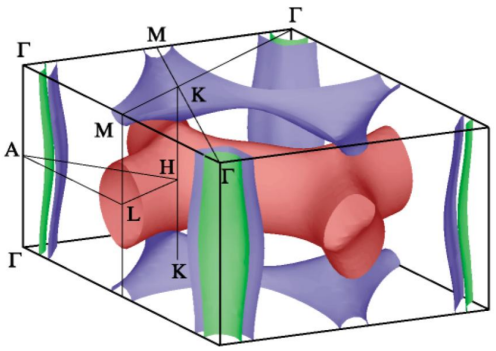

(b) The MgB_2 Fermi surface by Mazin and Antropov.[7]

Figure 1.1: (a) The unit cell [6] and (b) Fermi surface [7] of MgB_2. The layers of honeycomb-structured boron sheets alternate with layers of hexagonal magnesium. The π- and σ-bands form distinct surfaces, resulting in a Fermi surface with two sheets. The green and blue cylinders are formed from σ-bands, while the blue (bonding) and red (antibonding) tubular networks in the centre result from the π-bands.

The structure of magnesium diboride (Figure 1.1a) consists of alternating layers of magnesium and boron, with the B atoms forming honeycomb sheets similar to that of graphite sheets. The electronic states for MgB_2 are analogous to that of benzene, with σ-bands constricted to the planes of B sheets to form the covalent bonds with sp^2 hybridised boron orbitals. The π-bands, donated to by Mg layers, connect the B layers through layers of Mg with hybridised p_z orbitals. With very little electron hopping between these two bands, MgB_2 forms two Fermi surfaces which are essentially non-interacting.[8] This also leads to the formation of two distinct band gaps, creating difficulty in early attempts to accurately describe the superconductivity in the material.[9]

Further study revealed the presence of a particularly strong coupling E_{2g} phonon mode (see Figure 1.2). The E_{2g} mode referred to the in-plane vibration of the boron atoms and with the σ-band concentrated along the B-B axes, this phonon causes a significant distortion

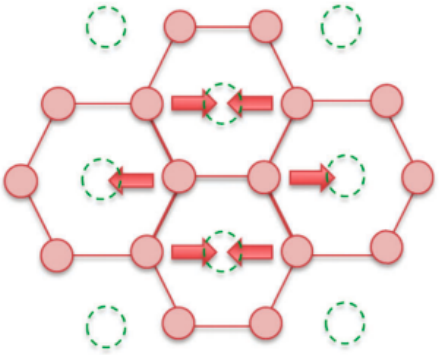

Figure 1.2: A diagram by Alarco et al.[10] representing the E_{2g} phonon vibrations (arrows) for MgB_2. The boron atoms (pink) shown make up honeycomb sheets, separated by magnesium (green) layers above and below the boron plane.

in the σ-band network. This shifts the electronic states to give strong electron-phonon coupling.[5]

Attempts to build on the discovery have continued over the past two decades, providing a wealth of research into layered structures and diborides [11, 12, 13, 14, 15, 16], as well as work on doping and pressurising MgB_2 in search of an improved T_c.[17, 18, 19, 20, 21, 22, 23, 24] For example, Johansson et al.[23] found that compression under hydrostatic pressure led to a decrease in T_c particularly due to compression in the c axis, reducing the interlayer separation. Conversely, expansion of the interlayer separation allowed for a small increase in T_c, considered to be a result of an increase in energy of the σ-band and a decrease in the frequency of the E_{2g} phonon mode. When focused on the *ab* plane, biaxial compressive strain leads to a reduction in the B-B length, resulting in an increased frequency of the E_{2g} mode, as well as a decrease in $N(E_f)$, both contributing to an overall reduction in the T_c. The reverse is true for biaxial tensile strain, with a reduced E_{2g} frequency and increased $N(E_f)$.[25]

Since the discovery of MgB_2 as a superconducting material, several applications have been implemented and suggested, including superconducting magnets for particle accelerators [26], levitation devices [27], and magnetic resonance imaging (MRI) technology [28], as well as wire and cable applications.[29] Furthermore, MgB_2 has been frequently used for the fabrication of superconducting quantum interference devices (SQUIDs).[30, 31]

1.3 Thesis Outline

The aim of this work is to use first principles electronic structure calculations to compute the superconducting transition temperature of magnesium diboride and a related compound. This will primarily be achieved with density functional theory through the CASTEP software package.[32]

Chapter 2

Beginning with an introduction to the many-body Schrödinger equation, this chapter encapsulates the approximations necessary to understand the density functional theory framework for ground state calculations. The use of Bloch functions is introduced to simplify materials using periodicity. Finally, the need for exchange correlation functionals is discussed, along with the use of pseudopotentials.

Chapter 3

Continuing the theory from the previous chapter, here we introduce density functional perturbation theory from lattice dynamics to give the foundations for computing phonons, going beyond the ground state configuration. The dynamical matrix is introduced before discussing the Eliashberg spectral function and the formalism required to calculate a critical temperature for a material.

Chapter 4

Crucial aspects of the computational method within CASTEP are discussed in greater detail, also including a summary of the entire workflow for finding the critical temperature for any input structure given. This includes details on optimising the structure, calculating the ground state energy, and computing the band structures, phonon modes, and electron-phonon matrix elements.

Chapter 5

Magnesium diboride is studied with the method provided by the previous section as an initial verification of the process. Structural, electronic, and vibrational properties are detailed before arriving at a predicted critical temperature with good agreement with experimental data.

Chapter 6

A new material, $LiAlB_4$, is introduced and studied with the same foci as for MgB_2,

culminating in the prediction of a critical temperature. Further details of the material are then discussed, such as possible effects of pressure, as well as insights from genetic algorithm energy-minimisation searches to confirm the most stable structure for the material.

Chapter 7

General conclusions are drawn from the work as a whole, discussing successes and limitations, along with suggestions for further work.

Chapter 2

Electronic Ground State Theory

"The underlying physical laws necessary for the mathematical theory of a large part of physics and the whole of chemistry are thus completely known, and the difficulty is only that the exact application of these laws leads to equations much too complicated to be soluble. It therefore becomes desirable that approximate practical methods of applying quantum mechanics should be developed, which can lead to an explanation of the main features of complex atomic systems without too much computation." [33]

– Paul Dirac, 1929.

2.1 Introduction

The study of the electronic structure of materials has seen rapid advancement within the past century, particularly with the introduction of computational physics. With the birth of quantum mechanics and the formulation of the Schrödinger equation, atomic interactions became understood on the atomic scale with greater detail. However, the computational intractability of the Schrödinger equation for any system of interest quickly led to the search for useful approximations. This chapter focuses on the development of these approximations from the many-body Schrödinger equation to a core understanding of density functional theory (DFT) as developed by Hohenberg, Kohn, and Sham.

The use of DFT within computational physics has become widespread, used within over 40,000 scientific papers produced annually by 2020.[34] Among computational approaches to approximating electronic states, DFT provides an accessible and inexpensive option while producing accurate results. For example, DFT achieved a 2.45% mean absolute relative error (MAE) in a study of the electric dipole polarisability gradient of methane,

compared to 1.57% for coupled cluster singles and doubles (CCSD).[35] However, DFT scales with respect to system size as $O(N^3)$, whereas a popular post-DFT method such as CCSD scales as $O(N^6)$. While CCSD is often capable of achieving improved accuracy, DFT consistently provides great accuracy with the capacity to scale to much larger systems.

2.2 The Schrödinger Equation

The Schrödinger equation provides a means to accurately describe the behaviour of a quantum mechanical system. The *time-dependent* Schrödinger equation takes the general form

$$i\hbar\frac{\partial}{\partial t}\Psi(\mathbf{r}_e,\mathbf{R}_n,t) = \hat{H}\Psi(\mathbf{r}_e,\mathbf{R}_n,t), \tag{2.1}$$

where $\hbar$ is the reduced Planck's constant, $\hat{H}$ is the Hamiltonian operator, and Ψ is the full many-body wavefunction, including both electronic and nuclear coordinates, which are denoted by $\mathbf{r}_e$ for electron e and $\mathbf{R}_n$ for nucleus n respectively. For a single particle, the Schrödinger equation takes the form

$$i\hbar\frac{\partial}{\partial t}\Psi(\mathbf{r},t) = \left[-\frac{\hbar^2}{2m}\nabla^2 + \hat{V}(\mathbf{r},t)\right]\Psi(\mathbf{r},t), \tag{2.2}$$

where $\hat{V}(\mathbf{r},t)$ represents the potential energy of any forces acting on the particle in its environment and m is the mass of the particle. Rather than solving this equation directly, it is simpler to solve for stationary states. Taking the case of time-independent potentials $\hat{V}(\mathbf{r},t) = \hat{V}(\mathbf{r})$, we can first break down the wavefunction into spatial and temporal parts:

$$\Psi(\mathbf{r},t) = \psi(\mathbf{r})f(t) \tag{2.3}$$

We divide both sides of Eq. (2.2) by $\psi(\mathbf{r})f(t)$ to obtain

$$i\hbar\frac{1}{f(t)}\frac{\partial f(t)}{\partial t} = \frac{1}{\psi(\mathbf{r})}\left[-\frac{\hbar^2}{2m}\nabla^2\psi(\mathbf{r}) + \hat{V}(\mathbf{r})\psi(\mathbf{r})\right]. \tag{2.4}$$

Given that the left-hand side is only dependent on time, while the right-hand side is only dependent on $\mathbf{r}$, we can equate both sides to a constant, E, which has dimensions of energy. The right-hand side can thus be written as the *time-independent* Schrödinger equation,

$$\hat{H}\psi(\mathbf{r}) = E\psi(\mathbf{r}), \tag{2.5}$$

where

$$\hat{H} = -\frac{\hbar^2}{2m}\nabla^2 + \hat{V}(\mathbf{r}) \tag{2.6}$$

To find solutions for the temporal part,

$$\begin{aligned} i\hbar\frac{1}{f(t)}\frac{df(t)}{dt} &= E \\ i\hbar\frac{1}{f(t)}df(t) &= Edt \\ \frac{1}{f(t)}df(t) &= \frac{E}{i\hbar}dt \\ \int\frac{1}{f(t)}df(t) &= \int -\frac{iE}{\hbar}dt \\ f(t) &= e^{-iEt/\hbar} \end{aligned} \tag{2.7}$$

Therefore, the state in Eq. (2.3) becomes the stationary state

$$\Psi(\mathbf{r},t) = \psi(\mathbf{r})e^{-iEt/\hbar}, \tag{2.8}$$

where the probability density $|\Psi(\mathbf{r},t)|^2 = |\psi(\mathbf{r})|^2$ does not depend on time.

For a system involving N electrons and M nuclei, we have the many-body Schrödinger equation

$$\hat{H}\psi(\mathbf{r}_1,...,\mathbf{r}_N,\mathbf{R}_1,...,\mathbf{R}_M) = E\psi(\mathbf{r}_1,...,\mathbf{r}_N,\mathbf{R}_1,...,\mathbf{R}_M), \tag{2.9}$$

with the Hamiltonian

$$\begin{aligned} \hat{H} &= \hat{T}^N + \hat{T}^e + \hat{V}^{NN} + \hat{V}^{Ne} + \hat{V}^{ee} \\ &= -\sum_I \frac{\hbar^2}{2M_I}\nabla^2_{\mathbf{R}_I} - \sum_i \frac{\hbar^2}{2m_e}\nabla^2_{\mathbf{r}_i} \\ &\quad + \frac{1}{2}\sum_I\sum_{J\neq I}\frac{Z_I Z_J e^2}{4\pi\varepsilon_0|\mathbf{R}_I - \mathbf{R}_J|} - \sum_I\sum_j \frac{Z_I e^2}{4\pi\varepsilon_0|\mathbf{R}_I - \mathbf{r}_j|} + \frac{1}{2}\sum_i\sum_{j\neq i}\frac{e^2}{4\pi\varepsilon_0|\mathbf{r}_i - \mathbf{r}_j|}. \end{aligned} \tag{2.10}$$

Here, $\hat{T}$ is the kinetic energy operator and $\hat{V}$ is the potential produced by nuclear-nuclear, nuclear-electron, and electron-electron Coulombic interactions. Z_I, M_I, and $\mathbf{R}_I$ are the atomic number, mass, and position of nucleus I respectively, while $\mathbf{r}_i$ is the position of electron i.

The energy of the system is given by the expectation value of the Hamiltonian, $\langle\hat{H}\rangle$. The variational principle states that for any trial wavefunction, the ground state energy is always less than or equal to the value of $\langle\hat{H}\rangle$ calculated with the trial wavefunction. Hence, the ground state of the system (the lowest energy) may be found by searching all possible wavefunctions to find the one which minimises the energy. As we cannot guarantee that the trial wavefunction is normalised, we introduce a normalisation factor, $\frac{1}{\langle\Psi|\Psi\rangle}$, which is

equal to one when we do have orthonormality. The ground state can therefore be found through

$$E_0 = \min_{\Psi} \frac{\langle \Psi | \hat{H} | \Psi \rangle}{\langle \Psi | \Psi \rangle}. \tag{2.11}$$

However, this is computationally intractable in practice – with the Schrödinger equation and Hamiltonian in $3M + 3N$ dimensions, the problem scales quickly as the system grows to any reasonable size for a real material. As such, any system more complex than a hydrogen atom cannot be solved analytically with the Schrödinger equation.

2.3 The Born-Oppenheimer Approximation

The Born-Oppenheimer approximation [36] separates the motion of nuclei and electrons on the basis of the large differential in mass (and by extension, velocities) between the two. As such, on the time-scale of nuclear motion, we consider the electrons to react quickly to find the ground state, with the nuclei treated as classical point particles. Following Byrne,[37], the Schrödinger equation can be separated into nuclear and electronic parts, while treating the nuclear positions as fixed external parameters:

$$\Psi(\{\mathbf{R}_I\}, \{\mathbf{r}_i\}) = \psi^N(\{\mathbf{R}_I\}) \times \psi^e_{\mathbf{R}}(\{\mathbf{r}_i\}). \tag{2.12}$$

The subscript R represents the parametric dependence of the electronic wavefunction on the nuclear coordinates. For the electronic part, with the nuclei treated as classical, fixed-point particles, $\hat{T}^N = 0$. Furthermore, $\hat{V}^{NN}$ becomes a constant which may shift the electronic energy but does not affect ψ^e. As such, this term can be included in either the electronic or nuclear wavefunctions. We can write an electronic Schrödinger equation as

$$\hat{H}^e_{\mathbf{R}} \psi^e_{\mathbf{R}}(\{\mathbf{r}_i\}) = E^e_{\mathbf{R}} \psi^e_{\mathbf{R}}(\{\mathbf{r}_i\}). \tag{2.13}$$

The electronic Hamiltonian, consisting of the parts of the total Hamiltonian which depend on electronic coordinates, can be expressed as

$$\hat{H}^e_{\mathbf{R}} = \hat{T}^e + \hat{V}^{Ne}_{\mathbf{R}} + \hat{V}^{ee}. \tag{2.14}$$

For the nuclear wavefunction, we consider the electronic energy, $E^e_{\mathbf{R}}$, as a potential energy surface on which the nuclei move, giving

$$\hat{H}^N = \hat{T}^N + \hat{V}^{NN} + E^e_{\mathbf{R}}. \tag{2.15}$$

Applying the full Hamiltonian to the whole wavefunction, we find through the product rule on both the first and second derivatives of $\hat{T}^N$ that the nuclear kinetic energy operator acts directly on the electronic wavefunction (here and henceforth using atomic units where $e = \hbar = m_e = 4\pi\varepsilon_0 = 1$):

$$\begin{aligned}
\hat{T}^N \psi^N \psi^e_{\mathbf{R}} &= -\sum_I \frac{1}{2M_I} \frac{\partial^2}{\partial \mathbf{R}_I^2} \psi^N \psi^e_{\mathbf{R}} \\
&= -\sum_I \frac{1}{2M_I} \frac{\partial}{\partial \mathbf{R}_I} \left(\frac{\partial \psi^N}{\partial \mathbf{R}_I} \psi^e_{\mathbf{R}} + \psi^N \frac{\partial \psi^e_{\mathbf{R}_I}}{\partial \mathbf{R}_I} \right) \\
&= -\sum_I \frac{1}{2M_I} \left[\frac{\partial^2 \psi^N}{\partial \mathbf{R}_I^2} \psi^e_{\mathbf{R}} + 2 \frac{\partial \psi^N}{\partial \mathbf{R}_I} \frac{\partial \psi^e_{\mathbf{R}}}{\partial \mathbf{R}_I} + \psi^N \frac{\partial^2 \psi^e_{\mathbf{R}_I}}{\partial \mathbf{R}_I^2} \right].
\end{aligned} \tag{2.16}$$

Then, the full Schrödinger equation can now be written as

$$\begin{aligned}
\hat{H}\Psi &= \left[-\sum_I \frac{1}{2M_I} \nabla^2_{\mathbf{R}} + \frac{1}{2} \sum_{J \neq I} \frac{Z_I Z_J}{|\mathbf{R}_I - \mathbf{R}_J|} + E^e_{\mathbf{R}} \right] \Psi \\
&= \psi^e_{\mathbf{R}} \left[-\sum_I \frac{1}{2M_I} \nabla^2_{\mathbf{R}} + \frac{1}{2} \sum_{J \neq I} \frac{Z_I Z_J}{|\mathbf{R}_I - \mathbf{R}_J|} + E^e_{\mathbf{R}} \right] \psi^N \\
&\quad -\sum_I \frac{1}{2M_I} \left[2 \frac{\partial \psi^N}{\partial \mathbf{R}_I} \frac{\partial \psi^e_{\mathbf{R}_I}}{\partial \mathbf{R}_I} + \psi^N \frac{\partial^2 \psi^e_{\mathbf{R}}}{\partial \mathbf{R}_I^2} \right].
\end{aligned} \tag{2.17}$$

The final line in Eq. (2.17) contains two terms which both couple the electronic and nuclear wavefunctions, known as the non-adiabatic terms. For the second of the non-adiabatic terms, Steinfeld [38] shows that we can loosely approximate the derivatives of $\mathbf{R}_I$ and $\mathbf{r}_i$, given that they operate over the approximately same atomic dimensions. With this, we obtain

$$\frac{1}{2M_I} \frac{\partial^2 \psi^e_{\mathbf{R}}}{\partial \mathbf{R}_I^2} \approx \frac{1}{2M_I} \frac{\partial^2 \psi^e_{\mathbf{R}}}{\partial \mathbf{r}_i^2} = \frac{p_e^2}{2M_I} \psi^e_{\mathbf{R}} = \frac{1}{M_I} E^e \psi^e_{\mathbf{R}}, \tag{2.18}$$

where p_e is the momentum of an electron. This term scales with the ratio of electronic mass to nuclear mass, typically on the order of 10^{-4} to 10^{-5}. Therefore, this term can generally be disregarded as negligible.[39]

For a stationary state, the first of the non-adiabatic terms is equivalent to the rate of change of the total charge of the system with respect to the nuclear coordinates, which is zero.[37] For a dynamical system, however, this term acts as a coupling between excitations of the nuclear and electronic wavefunctions, for which we define the electron-phonon

operator as

$$-\sum_I \frac{1}{M_I}\frac{\partial \psi^N}{\partial \mathbf{R}_I}\frac{\partial \psi^e_{\mathbf{R}_I}}{\partial \mathbf{R}_I} = \hat{H}^{ep}\psi^N\psi^e_{\mathbf{R}}, \tag{2.19}$$

acting on both the nuclear and electronic wavefunctions. For now, this electron-phonon coupling term can be ignored for the purpose of ground state electronic calculations, but this will be reintroduced through perturbation theory later. With the non-adiabatic terms ignored, we obtain the nuclear Schrödinger equation

$$\left[-\sum_I \frac{1}{2M_I}\nabla^2_{\mathbf{R}} + \frac{1}{2}\sum_I\sum_{J\neq I}\frac{Z_I Z_J}{|\mathbf{R}_I - \mathbf{R}_J|} + E^e_{\mathbf{R}}\right]\psi^N = E\psi^N. \tag{2.20}$$

The adiabatic principle crucially allows us to separate the nuclear and electronic motion, with a residual electron-phonon coupling term. It can be assumed for now that the electrons respond instantaneously to nuclear motion to occupy the ground state. The Born-Oppenheimer approximation can break down in certain situations, most notably if light elements are involved in the system, which reduces the effect of the m_e/M_I ratio. Furthermore, it breaks down in cases for which the nuclear derivative of the electronic wavefunction changes rapidly. For example, at conical intersections of potential energy surfaces, the coupling between nuclei and electrons becomes much more important, governing the non-adiabatic processes.

While the many-body Schrödinger equation has been simplified to a fixed nuclear potential, any system with more than a few electrons is still much too large, with a dimensionality of $3M$. This is primarily due to the electron-electron interactions, for which every pair of electrons is coupled, giving correlation between electron states. This term cannot be neglected for a real material system and so density functional theory will be introduced to manage this problem.

2.4 Density Functional Theory

Following from the Born-Oppenheimer approximation, we treat the Coulomb potential of the fixed nuclei as a static external potential,

$$\hat{V}_{ext} = \sum_i V_{ext}(\mathbf{r}) = -\sum_i\sum_J \frac{Z_J}{\mathbf{r}_i - \mathbf{R}_J}. \tag{2.21}$$

The remainder of $\hat{H}^e_{\mathbf{R}}$ is therefore

$$\hat{F} = \hat{T}^e + \hat{V}^{ee}, \tag{2.22}$$

such that

$$\hat{H} = \hat{F} + \hat{V}_{ext}. \tag{2.23}$$

Given that $\hat{F}$ is the same for all N-electron systems, $\hat{H}$ and the state $|\Psi\rangle$ are determined by $\hat{F}$ and N. As such, we describe the electronic density as

$$n(r) = \langle \Psi | \hat{n} | \Psi \rangle, \tag{2.24}$$

where

$$\hat{n} = \sum_i \delta(\mathbf{r} - \mathbf{r_i}). \tag{2.25}$$

Density functional theory (DFT) is based upon the Hohenberg-Kohn Theroems of 1964[40], which can be broken down into two key theorems:

1. In the ground state of a system, the electron density uniquely determines the external potential, $\hat{V}_{ext}$, within an additive constant.

2. The density of a system is the ground state if it minimises the variational energy of the system.

The first theorem is given by a proof by *reductio ad absurdum* in the seminal paper and can be described by

$$E_V[n] = \int V(\mathbf{r}) n(\mathbf{r}) d\mathbf{r} + F[n], \tag{2.26}$$

where $V(\mathbf{r})$ is an arbitrary potential. The second theorem can be proven with the variational principle on Eq. (2.26). While these theorems provide an avenue for calculating the ground state energy through the minimisation of $E_V[n]$, $F[n]$ is not explicitly known, so this is not straightforward.

The introduction of the Kohn-Sham equations [41] in the following year would become a major breakthrough for formalising DFT. These equations describe a system of non-interacting electrons in a fictitious potential, which gives the same ground-state density as the real system. $F[n]$ contains the electronic kinetic energy and the electron-electron interaction energy, which are difficult to evaluate or express in terms of $n(\mathbf{r})$. However, if exchange and correlation effects are neglected, the interaction energy becomes the classical Hartree term

$$E_{Hartree} = \frac{1}{2} \iint \frac{n(\mathbf{r}) n(\mathbf{r}')}{|\mathbf{r} - \mathbf{r}'|} d\mathbf{r} d\mathbf{r}'. \tag{2.27}$$

For a non-interacting system with the same density, the kinetic energy for independent

electrons with orbitals $\psi_i(\mathbf{r})$ is

$$T^{KS}[n] = -\frac{1}{2}\sum_{i}^{occ}\int \psi_i^*(\mathbf{r})\nabla^2\psi_i(\mathbf{r})d\mathbf{r} \tag{2.28}$$

and

$$n(\mathbf{r}) = 2\sum_{i}^{occ}\psi_i^*(\mathbf{r})\psi_i(\mathbf{r}). \tag{2.29}$$

where the factor of two comes from spin degeneracy, assuming the absence of magnetism. This assumption can be held for the rest of this work.

In the Kohn-Sham scheme, we then express Eq. (2.26) as

$$E_V[n] = \int V(\mathbf{r})n(\mathbf{r})d\mathbf{r} + T^{KS}[n] + E_{Hartree}[n] + E_{XC}[n], \tag{2.30}$$

where E_{XC} is known as the *exchange and correlation energy*. This term collects all of the unknowns into a single functional, containing electron-electron interaction energy beyond $E_{Hartree}$ and the difference between the sum of the independent kinetic energy operators and the many-body kinetic operator. This will be discussed in greater detail in the following section. Still, the question remains as to how the electron density itself should be calculated. Making use of the second Hohenberg Kohn theorem, the ground-state density will be the function that minimises the energy:

$$\left.\frac{\delta E_V[n]}{\delta n(\mathbf{r})}\right|_{n_0} = 0, \tag{2.31}$$

where n_0 gives a constraint to maintain the integrated number of electrons. This allows us to write the Kohn-Sham equations, a set of coupled single-particle equations:

$$E_i\psi_i(\mathbf{r}) = \left[-\frac{1}{2}\nabla^2 + V_{ext}(\mathbf{r}) + V_H(\mathbf{r}) + V_{XC}(\mathbf{r})\right]\psi_i, \tag{2.32}$$

where V_H is the Hartree potential

$$V_H(\mathbf{r}) = \int \frac{n(\mathbf{r}')}{|\mathbf{r}-\mathbf{r}'|}d\mathbf{r}' \tag{2.33}$$

and V_{XC} is the *exchange and correlation potential* (XC), defined by

$$V_{XC}(\mathbf{r}) = \left.\frac{\delta E_{XC}[n]}{\delta n(\mathbf{r})}\right|_{n(\mathbf{r})}. \tag{2.34}$$

The Hartree potential represents the classical potential of a charge distribution in the

system, but includes an electron self-interaction energy which must be removed through the XC functional. If we knew the XC functional we could calculate the total energy of the system using the electron density. This is the next problem to solve, as an exact form of this is not known, so we must instead construct approximations.

2.5 Exchange-Correlation Functionals

The exchange and correlation energy can be generally described by

$$E_{XC} = T - T^{KS} + E^{ee} - E_H, \tag{2.35}$$

where T is the exact many-body kinetic energy, T^{KS} is the Kohn-Sham kinetic energy for the Kohn-Sham orbitals, and E^{ee} is the exact electron-electron interaction energy. Therefore, the XC functional is essentially a term containing the differences between the time-independent Schrödinger equation and the Kohn-Sham equations. It is helpful to first clarify the terms exchange and correlation here.

Electron exchange is underpinned by the Pauli exclusion principle, stating that no two fermions can be in the same quantum state. In practice, this means that only two electrons may occupy an orbital, provided they have opposite spin. This is enforced by the necessity for the electronic wavefunction to be antisymmetric with respect to the interchange of electrons, as they are identical fermions. The exchange energy is given by

$$E_X = -\frac{1}{2}\sum_{i,j}\iint \psi_i^*(\mathbf{r}_1)\psi_j^*(\mathbf{r}_2)\frac{1}{|\mathbf{r}_1-\mathbf{r}_2|}\psi_i(\mathbf{r}_2)\psi_j(\mathbf{r}_1)d\mathbf{r}_1 d\mathbf{r}_2. \tag{2.36}$$

The concept of exchange was initially introduced through Hartree-Fock (HF) theory, which allows us to describe a wavefunction through a single determinant, the Slater determinant.[42, 43, 44] The HF Hamiltonian is

$$\hat{H}_{HF} = -\frac{1}{2}\nabla^2 + V_{ext}(\mathbf{r}) + V_H(\mathbf{r}) + E_X \tag{2.37}$$

While the exchange energy only affects electrons of the same spin, the correlation energy affects all electrons and is more complex, lacking an analytic expression. It is essentially the difference between the non-interacting system in the HF approximation (which includes an exchange term, but does not consider correlation) and the true interacting system according to the many-body Schrödinger equation. For the latter, there is a reduced probability of electrons being found in close proximity of each other, the electrons have correlated positions, and the electronic wavefunction contains a greater number of degrees

of freedom. Calculating the correlation energy exactly would be about as computationally expensive as solving the Schrödinger equation itself, so this must be approximated.

For a system with many electrons, both the correlation and the exchange energies are approximated within the XC functional for computational feasibility. Generally, we can write the exchange and correlation energy as

$$E_{XC}[n] = \frac{1}{2}\iint n(\mathbf{r})\frac{n_{XC}(\mathbf{r},\mathbf{r}')}{|\mathbf{r}-\mathbf{r}'|}d\mathbf{r}, \tag{2.38}$$

where n_{XC} is an unknown, describing the interaction of an electron at $\mathbf{r}$ and its exchange-correlation hole at $\mathbf{r}'$. The exchange-correlation hole describes the electron density that would be missing around an electron if all other electrons were removed. The sum rule dictates that this should integrate to one electron

$$\int n_{XC}(\mathbf{r},\mathbf{r}')d\mathbf{r}' = -1, \tag{2.39}$$

although the shape of the hole is unknown.

The first XC functional, the local density approximation (LDA), was introduced by Kohn and Sham in the same year as the Kohn-Sham equations.[41] This remains a commonly used functional due to its remarkable performance despite its simplicity. The approximation states that the exchange and correlation energy density for an electron at point $\mathbf{r}$ where the density is $n(\mathbf{r})$ is the same as that for a homogeneous electron gas (HEG) with the same density. The LDA functional therefore takes the form

$$E_{XC}^{LDA}[n] = \int n(\mathbf{r})\varepsilon_{XC}^{HEG}(n(\mathbf{r}))d\mathbf{r}, \tag{2.40}$$

where ε_{XC}^{HEG} is the exchange and correlation energy density for a HEG of density $n(\mathbf{r})$. This functional assumes the hole is spherical and obeys the sum rule, which grants it such success. This approximation is exact for systems which have a very slowly varying density, yet many systems of interest have a rapidly varying density. As such, it maintains a good level of accuracy for many simple systems, such as metals. On the other hand, it has a tendency to over-bind atoms to give shorter, stronger bonds and smaller lattice parameters.[45]

An expansion on this local approximation is the generalised-gradient approximation (GGA), which includes both the density at $\mathbf{r}$ and its derivative, with the general form

$$E_{XC}^{GGA}[n] = \int n(\mathbf{r})\varepsilon_{XC}^{GGA}(n(\mathbf{r},\nabla)n(\mathbf{r}))d\mathbf{r}. \tag{2.41}$$

In the past few decades, there have been a number of functionals using this framework [46, 47, 48], as well as some which combine GGA exchange with LDA and/or Hartree-Fock correlation [49], however, this work will use the functional developed by Perdew, Burke, and Ernzerhof (PBE).[50] PBE remains to be a staple GGA, maintaining simplicity while granting the improved features of GGAs. Generally, GGA functionals have the opposite tendency to LDA in that they may under-bind atoms to give longer, weaker bonds.[51] Unless otherwise stated, PBE will be used for calculations within this work.

2.6 Bloch's Theorem and Plane Waves

We now have the formalism required to effectively approximate the Schrödinger equation for simple systems of a small number of electrons, which will work well for many atoms and molecular structures. When working with bulk materials, we still have an issue, given that the number of electrons in any macroscopic sample of a material can be on the order of 10^{24}. In the study of bulk crystals, materials can extend *ad infinitum*, however, a vast majority of these will have translation symmetry, giving periodicity. With this, the infinite crystal can be reduced to a finite repeating unit cell of a generally small number of atoms and therefore a reasonable number of electrons.

This concept is summarised in Bloch's theorem, a fundamental idea in condensed matter physics, stating that if the nuclei are arranged periodically, then the potential and density must also be periodic:

$$V(\mathbf{r}+\mathbf{L}) = V(\mathbf{r}), \tag{2.42}$$

where L is a lattice vector. To exploit this periodicity of crystal systems, we write the wavefunction as a set of Bloch waves

$$\psi_{\mathbf{k}}(\mathbf{r}) = e^{i\mathbf{k}.\mathbf{r}} u_{\mathbf{k}}(\mathbf{r}) \tag{2.43}$$

where $\mathbf{k}$ is a wavevector, $u_{\mathbf{k}}(\mathbf{r}+\mathbf{L}) = u_{\mathbf{k}}(\mathbf{r})$ is a cell-periodic function, and $e^{i\mathbf{k}.\mathbf{r}}$ is an arbitrary phase factor. The phase factor describes the phase change from one unit cell to the next.

We can express this quasi-periodic function as a 3D Fourier series:

$$\psi_{\mathbf{k}}(\mathbf{r}) = \sum_{\mathbf{G}} c_{\mathbf{G}\mathbf{k}} e^{i(\mathbf{G}+\mathbf{k}).\mathbf{r}}, \tag{2.44}$$

where $c_{\mathbf{G}\mathbf{k}}$ are unknown complex coefficients and wavevectors $\mathbf{G}$ are reciprocal lattice vectors. $\mathbf{G}$-vectors form the basis of the reciprocal lattice, related to the real-space lattice

vectors, $\mathbf{L}$, by $e^{i(\mathbf{G}.\mathbf{L})} = 1$, enforcing periodicity in reciprocal space.

Now, instead of having to solve an equation for a wavefunction over all space, the problem is reduced to solving a set of wavefunctions in a single unit cell (or supercell). Yet, this currently requires calculations for every value of $\mathbf{k}$. To restrict these values, we impose boundary conditions for which $\mathbf{k}$ is limited to the first Brillouin zone (BZ), which is the volume of reciprocal space around the origin including all points which are closer to the origin than to any other $\mathbf{G}$-vector. The solutions to $\psi_{\mathbf{k}}$ outside of this are degenerate with those inside due to periodicity. This set can be further reduced to a finite set of points within the first BZ, owing to the fact that the wavefunctions vary smoothly through the first BZ [52], allowing us to choose a set of points and extrapolate approximations between them.[53] The number of k-points required scales with the size of the first BZ and, therefore, inversely with the size of the real-space cell. The k-point sampling of the first BZ is an important input parameter in CASTEP calculations, which will be discussed in the following chapter.

Finally, we must determine the values of $\mathbf{G}$. As reciprocal space vectors within the first BZ, the smallest non-zero $\mathbf{G}$ can be given by the largest wavelength in real space which is periodic with the unit cell length:

$$\mathbf{G}_{min} = \frac{2\pi}{a}, \tag{2.45}$$

where a is the length of the lattice vector for the material. In practice, the coefficients $c_{\mathbf{Gk}}$ associated with larger $\mathbf{G}$ values become smaller. This corresponds to the finer real-space resolution in the density description, where a larger $\mathbf{G}$ has an increasingly neglible effect on $\psi_{\mathbf{k}}$ and therefore on the properties. As such, we can truncate the set of $\mathbf{G}$ values at some point $\mathbf{G}_{max}$ and express this as a cut-off energy,

$$E_{cut} = \frac{1}{2m}|\mathbf{G}_{max}|^2. \tag{2.46}$$

The cut-off energy is the second key parameter alongside the k-point sampling.

2.7 Pseudopotentials

The final approximation made for ground state calculations lies in the pseudopotential approximation. The core of an atom consists of tightly bound and highly localised electrons and a strong nuclear Coulomb potential. Wavefunctions within the Kohn-Sham scheme must be orthonormal and, with core states being highly localised, valence states must oscillate with high frequency to remain orthogonal to core states. Modelling this

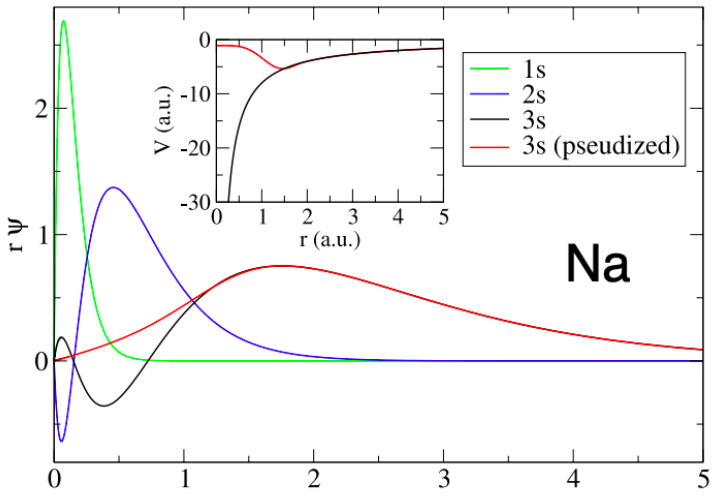

Figure 2.1: The pseudopotential approximation represented for a sodium atom by Dan Jones.[54]

rapid oscillation would be computationally taxing, requiring a larger basis set, so an approximation is encouraged. Given that the core electrons are relatively indifferent to the chemical environment and they contribute little to bonding, the potential can be combined with the nuclear potential to give an ionic pseudopotential. Furthermore, the valence electronic wavefunctions can be replaced by pseudowavefunctions, varying smoothly in the core region rather than maintaining the rapid oscillation.

In practice, this allows for pre-computed core electrons, which are entered into calculations through the pseudopotential. Still, the pseudopotential must obey some rules to provide accurate modelling:

$$\phi^{PS}(r > r_c) = \psi^{KS}(r > r_c) \tag{2.47}$$

$$\varepsilon_i^{PS} = \varepsilon_i^{KS} \tag{2.48}$$

Here, ϕ^{PS} is the pseudowavefunction. The first of these requires that the pseudowavefunction is identical to the all-electron Kohn-Sham wavefunction outside off a cut-off radius, r_c. The second requires the eigenvalues of the pseudowavefunction (ε_i^{PS}) to be identical to those of the Kohn-Sham wavefunction (ε_i^{KS}), providing the same energy. Furthermore, the pseudopotential must be able to reproduce the scattering properties of the original Coulomb potential.

To satisfy these rules, the norm of each pseudowavefunction should be identical to the Kohn-Sham wavefunction within r_c. For this to be true, the integrals of the square

amplitudes of the two must be equal [55]:

$$\int_0^{r_c} |\phi^{PS}(\mathbf{r})|^2 d\mathbf{r} = \int_0^{r_c} |\psi^{KS}(\mathbf{r})|^2 d\mathbf{r}. \tag{2.49}$$

This maintains the normalisation of wavefunctions and ensures that the total charge in the core is correct. Pseudopotentials that are generated according to this principle are known as norm-conserving pseudopotentials (NCPs).

While there are other methods of generating pseudopotentials, such as ultrasoft pseudopotentials [56], these are more difficult to compute. CASTEP calculations on phonons do not have full compatibility with USPs (while the finite displacement method is viable, linear response is not), therefore they will not be used in this work. We now have a framework to describe a periodic crystal in the Kohn-Sham scheme as a set of core ions and their valence electrons. From this point, it can be assumed unless otherwise stated that NCPs are used for any calculation.

Chapter 3

Lattice Dynamics and Electron-Phonon Theory

3.1 Introduction

While we now have everything required to calculate ground state systems to find lattice constants, electronic band structures, and more, dynamic interactions are not yet calculable. In the context of BCS superconductivity, phonons and the subsequent electron-phonon interactions are crucial to studying superconducting properties. A phonon can be defined as a quantised mode of vibration in a crystal lattice, for which the involved atoms collectively oscillate at the same frequency. They can be described by momentum, $\hbar\mathbf{q}$, and energy, $\hbar\omega$. In essence, they are the equivalent to the photon description of light, but instead describing sound. This chapter will discuss lattice dynamics and density functional perturbation theory, which will allow us to model phonon modes of materials and how this affects the ground state. We will then come to the reintroduction of the electron-phonon operator that had been dismissed for most of the previous chapter and see how this can be understood to predict a superconducting critical temperature.

3.2 Lattice Dynamics

As discussed with the Born-Oppenheimer approximation (Chapter 2.3), nuclei move on a much longer timescale than electrons. To accurately simulate the time evolution of a phonon mode, a large number of small time steps are required to effectively capture energy exchanges and to conserve the energy of the system. This would have to be repeated for a number of phonon modes to accurately model the vibrations in the material. As such,

approximations must again be invoked to simplify the nature of the calculations. First, we assume that the mean equilibrium position position of each ion, I, is a Bravais lattice site, $\mathbf{R}_I$. The lattice dynamics are simplified significantly by assuming that the amplitude of atomic displacements is small compared to the inter-atomic distances. This leads us to the harmonic approximation, where the N-ion harmonic crystal can be described as $3N$ independent harmonic oscillators.

We can break down the position of an atom in the crystal as a sum of the unit cell lattice vector, $\mathbf{R}_l$, and the position of the atom within that unit cell, τ_s. Here, l denotes the unit cell and s denotes the atom within that unit cell, such that $I = (l,s)$. Under thermal motion, we can then describe the actual position of the atom as

$$\mathbf{R}_I = \mathbf{R}_l + \tau_s + \mu_I, \tag{3.1}$$

where μ is the displacement from the equilibrium position.

For the total energy of E_0 at the equilibrium structural coordinates, we expand in a Taylor series in the atomic displacement, μ, giving

$$E = E_0 + \sum_{I,\alpha} \frac{\partial E}{\partial \mu_{I,\alpha}} \mu_{I,\alpha} + \frac{1}{2!} \sum_{I,\alpha,J,\beta} \frac{\partial^2 E}{\partial \mu_{I,\alpha} \mu_{J,\beta}} \mu_{I,\alpha} \mu_{J,\beta} + ..., \tag{3.2}$$

where α and β are Cartesian directions, with the 3rd order and higher order terms considered negligible within the harmonic approximation. At equilibrium, the forces on any atom are zero, therefore the first order derivative is zero, reducing Eq. (3.2) to

$$E \approx E_0 + \frac{1}{2} \sum_{I,\alpha,J,\beta} \frac{\partial^2 E}{\partial \mu_{I,\alpha} \mu_{J,\beta}} \mu_{I,\alpha} \mu_{J,\beta}. \tag{3.3}$$

The second derivatives describe the force constant matrix (FCM), representing all effective 3D spring constants between the atoms:

$$\begin{aligned} \Phi^{I,J}_{\alpha,\beta} &= \frac{\partial^2 E}{\partial \mu_{I,\alpha} \partial \mu_{J,\beta}} \\ &= -\frac{\partial F_{\mu_{I,\alpha,a}}}{\partial \mu_{J,\beta,a}}. \end{aligned} \tag{3.4}$$

Physically, $\Phi^{I,J}_{\alpha,\beta}$ is the atomic force constant in the α direction on atom I when atom J is displaced in the β direction.[4] Using Eq. (3.4), FCMs can be computed using the finite displacement method, wherein atoms are shifted from their equilibrium position by a small amount before evaluating forces on the perturbed configuration. This can be

used in cases where a perturbative approach is not appropriate, for example, if an ultrasoft pseudopotential is necessary.

Solving the FCM for all pairs of atoms in the material would be computationally intractable, so we apply the Born-von Karman boundary conditions. With a very large crystal, we can assume that displacements from phonons will repeat across an integer number of unit cells along the axes, $T = (T_a, T_b, T_c)$. Through Bloch's theorem, the allowed phonon modes are

$$\mu_{l-m,s} = e^{i\mathbf{q}.\mathbf{R}_m}\mu_{l,s}, \tag{3.5}$$

where l, m are unit cell indexes, s is still the atom index, and $\mathbf{R}_m$ is a vector to the origin of unit cell m. The phonon wavevectors are

$$\begin{aligned} q &= \left(\frac{2\pi}{T_a}, \frac{2\pi}{T_b}, \frac{2\pi}{T_c}\right) \\ &= \left(\frac{2\pi n_a}{L_a}, \frac{2\pi n_b}{L_b}, \frac{2\pi n_c}{L_c}\right), \end{aligned} \tag{3.6}$$

where n_x are integers and as $L \to \infty$, q becomes a continuum.[37] The wavelength of a phonon is simply $\lambda = \frac{2\pi}{|q|}$. As the restoring forces only depend on relative position, not absolute position, they can only depend on the vector between given atoms. Hence, the FCM can be rewritten as

$$\Phi^{I,J}_{\alpha,\beta} = \Phi^{s,t}_{\alpha,\beta}(l-m) \tag{3.7}$$

where the constants rely on the differences of l and m rather than depending on them directly.

Representing the force constant matrix in reciprocal space through a Fourier transform gives the dynamical matrix,

$$\begin{aligned} D^{s,t}_{\alpha,\beta}(\mathbf{q}) &= \frac{1}{N}\sum_m \Phi^{s,t}_{\alpha,\beta}(l-m)e^{i\mathbf{q}.(\mathbf{R}_l-\mathbf{R}_m)} \\ &= \sum_l \Phi^{s,t}_{\alpha,\beta}(l)e^{i\mathbf{q}.\mathbf{R}_l} \end{aligned} \tag{3.8}$$

where N is the number of atoms, m is the unit cell index for atom J, and the second line is given by translational invariance.

We must now look for the solutions to the dynamical matrix. From the equation of classical motion, we have

$$M_I\ddot{\mu}_{I,\alpha} = -\sum_{J,\beta}\Phi^{s,t}_{\alpha,\beta}(l-m)\mu_{J,\beta}. \tag{3.9}$$

Looking for plane wave solutions to the dynamical matrix, we can describe the atomic displacements as

$$\mu_{I,\alpha} = \frac{1}{2\sqrt{M_I}}\varepsilon_{I,\alpha}(\mathbf{q})e^{i(\mathbf{q}.\mathbf{R}_l-\omega t)}, \tag{3.10}$$

where $\varepsilon_I(\mathbf{q})$ are the phonon eigenvectors and ω is the phonon frequency. Substituting this into the equation of motion, we obtain

$$\begin{aligned}
M_I\frac{\partial^2}{\partial t^2}\frac{1}{2\sqrt{M_I}}\varepsilon_{I,\alpha}(\mathbf{q})e^{i(\mathbf{q}.\mathbf{R}_l-\omega t)} &= -\sum_{J,\beta}\Phi^{s,t}_{\alpha,\beta}(l-m)\frac{1}{2\sqrt{M_J}}\varepsilon_{J,\beta}(\mathbf{q})e^{i(\mathbf{q}.\mathbf{R}_m-\omega t)} \\
\sqrt{M_I}\omega^2\varepsilon_{I,\alpha}(\mathbf{q})e^{i(\mathbf{q}.\mathbf{R}_l-\omega t)} &= \sum_{J,\beta}\frac{1}{\sqrt{M_J}}\Phi^{s,t}_{\alpha,\beta}\varepsilon_{J,\beta}(\mathbf{q})e^{i(\mathbf{q}.\mathbf{R}_m-\omega t)} \\
\omega^2\varepsilon_{I,\alpha}(\mathbf{q}) &= \sum_{J,\beta}\frac{1}{\sqrt{M_IM_J}}\Phi^{s,t}_{\alpha,\beta}\varepsilon_{J,\beta}(\mathbf{q})e^{i\mathbf{q}.(\mathbf{R}_l-\mathbf{R}_m)} \\
\omega^2\varepsilon_{I,\alpha}(\mathbf{q}) &= \sum_{J,\beta}\frac{1}{\sqrt{M_IM_J}}D^{s,t}_{\alpha,\beta}(\mathbf{q})\varepsilon_{J,\beta}(\mathbf{q}).
\end{aligned} \tag{3.11}$$

Solving this equation gives both the phonon mode eigenvectors $\varepsilon_{I,\alpha}$ and the squared mode frequencies ω^2. Similarly to the electronic case, the problem is now reduced to calculating eigenvectors at a range of sampled q-points within the first BZ and then invoking Bloch's theorem with Eq. (3.5).

3.3 Density Functional Perturbation Theory

To construct the FCM and, consequently, the dynamical matrix, we require the second derivatives of energy. This can be achieved through the Hellmann-Feynman theorem [57], which relates the derivative of the energy to the expectation value of the derivative of the Hamiltonian with respect to some parameter, λ:

$$\frac{\partial E}{\partial \lambda} = \langle\psi|\frac{\partial \hat{H}}{\partial \lambda}|\psi\rangle, \tag{3.12}$$

where the Hamiltonian in this case is

$$\hat{H} = -\frac{1}{2}\nabla^2 + V^{KS} \tag{3.13}$$

and the parameter λ is ionic displacement from equilibrium, μ. V^{KS} is simply the sum of the potentials in the Kohn-Sham Hamiltonian: V_{ext}, V_H, and V_{XC}. The first term of this Hamiltonian does not depend on μ, therefore, by substituting Eq. (3.13) into Eq. (3.12)

and taking the negative of the derivative to describe the force, we have

$$F = -\frac{\partial E}{\partial \mu} = -\langle \psi | \frac{\partial V^{KS}}{\partial \mu} | \psi \rangle . \tag{3.14}$$

The second derivative is given by

$$k = \frac{\partial^2 E}{\partial \mu^2} = -\frac{\partial F}{\partial \mu} = \langle \frac{\partial \psi}{\partial \mu} | \frac{\partial V^{KS}}{\partial \mu} | \psi \rangle + \langle \psi | \frac{\partial V^{KS}}{\partial \mu} | \frac{\partial \psi}{\partial \mu} \rangle - \langle \psi | \frac{\partial^2 V^{KS}}{\partial \mu^2} | \psi \rangle , \tag{3.15}$$

for which none of the terms vanish and the linear response of the wavefunction with respect to perturbation is required. According to the $2n+1$ theorem [58], the n^{th} derivative of a wavefunction is needed to compute up to the $2n+1^{th}$ derivative of energy. As such, the second order derivatives require $n = 1$.

In density functional perturbation theory, we require the first order orbitals with respect to displacement, $\phi^{(1)}$. In this case, μ is the displacement of atoms with wavevector $\mathbf{q}$, where $\phi^{(1)}$ will have a Bloch-like wavefunction of the form

$$\phi^{(1)}_{\mathbf{k},\mathbf{q}}(\mathbf{r}) = e^{-i(\mathbf{k}+\mathbf{q}).\mathbf{r}} u^{(1)}(\mathbf{r}), \tag{3.16}$$

where $u^{(1)}(\mathbf{r})$ has the periodicity of the unit cell.

The first order response orbitals can be found through expanding the Schrödinger equation in terms of powers of μ and identifying linear terms. This is known as the Sternheimer equation,

$$(\hat{H}^{(0)} - \varepsilon^{(0)}_n) | \phi^{(1)}_n \rangle = -V^{KS(1)} | \phi^{(0)}_n \rangle . \tag{3.17}$$

The first order potential $V^{KS(1)}$ includes response terms of the Hartree and XC potentials and, therefore, depends on the first order density $n^{(1)}(\mathbf{r})$. This in turn depends on $\phi^{(1)}$, creating a self-consistent problem in finding $\phi^{(1)}$. CASTEP has two approaches to this problem - variational DFPT and the Green's function method suggested by Baroni.[59] The former operates through minimising the second order perturbation in the total energy to give the first order changes in the wavefunction, however, it is not variational for metals and, as such, cannot be used for superconductors. As such, the Green's function method is used here, which solves the Sternheimer equation in a self-consistent loop with first order density mixing. Density mixing involves mixing output densities with a new trial density for each sequential cycle. This is often employed within ground state calculations as well, with a range of mixing schemes available.

Whereas the finite displacement method only works at $\mathbf{q} = 0$, DFPT can calculate

responses to incommensurate $\mathbf{q}$. However, it does require the derivatives for the XC functional, limiting the choice of the functional. Furthermore, it is limited to using NCPs within CASTEP, as stated previously.

3.4 Electron-Phonon Coupling

At this point, we must now reintroduce the electron-phonon term as described by Eq. (2.19) that has, thus far, been neglected. With its dependency on the rate of change of the electronic wavefunction with respect to changes in the nuclear positions, it describes the coupling between excited nuclear and electronic states. As demonstrated by Byrne [37], we can avoid applying $\hat{H}^{ep}$ and instead look at the first-order nuclear-electron potential in the system. At the most basic approximation, this takes the direct change in the ionic potential due to the perturbation, known as the bare potential. In solids, particularly for metals, this bare potential is screened by other electrons in the system. Therefore, it is much more accurate to account for the reaction of electrons moving in response to the changing potential. This can be described by

$$\delta V_{\mathbf{q},j} = \sum_I \delta\tilde{\varepsilon}_{\mathbf{q},j,I} . \frac{\partial V_{\mathbf{q}}^{SCF}}{\partial \mu_I}, \tag{3.18}$$

where $\tilde{\varepsilon}_{\mathbf{q},j,I}$ is the mass reduced phonon eigenvector of atom I for the phonon $\mathbf{q}, j$ and $V_{\mathbf{q}}^{SCF}$ is the self-consistent potential derived from perturbative calculations.

The basic electron-phonon scattering process, often referred to as the electron-phonon vertex g [60], can be described by the Feynman diagrams represented in Figure 3.1.

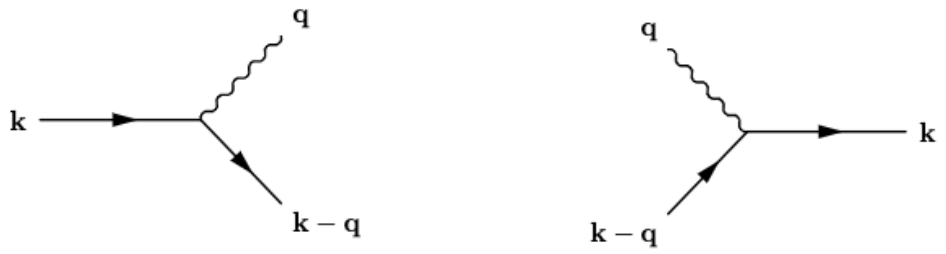

(a) Emission (b) Absorption

Figure 3.1: The emission and absorption of a phonon by an electron, forming an electron-phonon vertex in which the electron is scattered.

The electron-phonon matrix element, $g^{\mathbf{q},j}_{\mathbf{k},i,\mathbf{k}',i'}$, represents the scattering of an electron $|\mathbf{k}', i'\rangle$ from/to a state $|\mathbf{k}, i\rangle$ due to the absorption/emission of a phonon $\mathbf{q}, j$. Here, $\mathbf{q}$ describes the phonon wavevector for the mode j. Maintaining the conservation of

momentum gives the relationship $\mathbf{k}' = \mathbf{k} + \mathbf{q}$. We describe the matrix elements with

$$g^{\mathbf{q},j}_{\mathbf{k},i,\mathbf{k}',i'} = \sqrt{\frac{\hbar}{2\omega_{\mathbf{q},j}}} \langle \mathbf{k}', i' | \, \delta V^{SCF}_{\mathbf{q}} \, | \mathbf{k}, i \rangle \,, \tag{3.19}$$

where $\delta V^{SCF}_{\mathbf{q}}$ is the derivative of the self-consistent potential with respect to atomic positions and $\omega_{\mathbf{q},j}$ are the phonon frequencies.

The Eliashberg spectral function, $\alpha^2F(\omega)$, takes the sum over all the matrix elements for the interactions of all electronic states with phonons of frequency ω. Many variations of this function can be found in the literature, but here we apply Byrne's interpretation [37]:

$$\alpha^2F(\omega) = \frac{1}{N_f} \sum_{\mathbf{q},j} \sum_{\mathbf{k},i,\mathbf{k}',i'} |g^{\mathbf{q},j}_{\mathbf{k},i,\mathbf{k}',i'}|^2 \delta(\varepsilon_f - \varepsilon_{\mathbf{k},i}) \delta(\varepsilon_f - \varepsilon_{\mathbf{k}',i'}) \delta(\hbar\omega - \hbar\omega_{\mathbf{q},j}) \tag{3.20}$$

This expression takes a sum over every possible initial and final state, whilst restricting these to only electrons lying on the Fermi surface, ε_f, by using delta functions, similarly to the 'double-delta function' approximation. The third delta function constrains the phonon frequencies to $\omega_{\mathbf{q},j}$. Physically, the Eliashberg spectral function is proportional to the scattering rate of electrons due to the absorption/emission of a phonon of frequency $\omega_{\mathbf{q},j}$, giving an indicator of the overall strength of the scattering from the probabilities of the matrix elements. The indirect interactions of electrons through electron-phonon interactions lay the foundation for the formation of Cooper pairs in BCS theory.

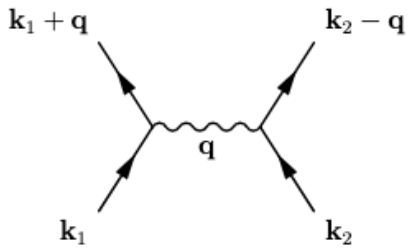

Figure 3.2: Electron-electron interaction facilitated by the exchange of a virtual phonon.

From this, we can obtain the electron-phonon coupling constant, λ, a dimensionless indicator of the strength of the electron-phonon interactions in the material. This is given by

$$\lambda = 2 \int \frac{\alpha^2F(\omega)}{\omega} d\omega. \tag{3.21}$$

McMillan pioneered the development in relating this constant to the superconducting transition temperature, or critical temperature, T_c.[61] By using the Debye temperature,

Θ_D and a Coulombic repulsion term, μ^*, he expressed the critical temperature as

$$T_c = \frac{\Theta_D}{1.45} \exp\left(\frac{-1.04(1+\lambda)}{\lambda - \mu^*(1+0.62\lambda)}\right). \tag{3.22}$$

The most significant uncertainty in this equation lies with the value of μ^*, which is difficult to calculate analytically and requires the use of tunneling experiments to find an accurate value experimentally. Therefore, μ^* is largely considered an adjustable parameter, though there is some disagreement on the range of values for which it may take. While McMillan [61] suggests a range of 0.1–0.2, modern approaches generally consider the acceptable range for conventional superconductors to be 0.10–0.15, though the upper limit may vary.[4, 62]

Allen and Dynes [63] continued McMillan's work and showed that the prefactor involving the Debye temperature can be replaced using a logarithmically averaged phonon frequency, ω_{log}, to give a similar equation

$$T_c = \frac{\omega_{log}}{1.2} \exp\left(\frac{-1.04(1+\lambda)}{\lambda - \mu^*(1+0.62\lambda)}\right), \tag{3.23}$$

where ω_{log} is given by

$$\omega_{log} = \exp\left[\frac{2}{\lambda}\int_0^\infty \frac{\alpha^2 F(\omega)\ln(\omega)}{\omega} d\omega\right]. \tag{3.24}$$

The Allen-Dynes equation is accurate for $\lambda < 1.5$, accounting for many instances of conventional superconductors, including those studied within this work. Henceforth, Eq. (3.23) will be used for all following T_c calculations made. From Eq. (1.3), we can deduce that $N(E_f)$ can be considered an approximate early indicator of the value of T_c, which can be computed with little effort. This has been used previously within high-throughput predictions for superconducting critical temperatures of structural analogues.[64, 65] These works are based on the Fröhlich model, relating $N(E_f)$ to T_c through

$$T_c \propto \frac{N(E_f)}{\sqrt{M}}, \tag{3.25}$$

where M is the mass of the formula unit.

Chapter 4

Computational Method

"This is a place where the relationship of physics and computation has turned itself the other way and told us something about the possibilities of computation. So this is an interesting subject because it tells us something about computer rules, and might tell us something about physics." [66]

– Richard Feynman, 1982.

4.1 Introduction

While Chapters 1 and 2 have covered the foundational theory for using DFT calculations to predict T_c, there are a number of practical considerations to acknowledge. Byrne's work [37] covers this in great detail, including the development of the computational framework for calculating electron-phonon coupling matrices in CASTEP. Here, the practical aspects will be minimised to crucial details for accurately repeating this method. The entire process is summarised in Figure 4.1 and will be expanded upon in this chapter.

The chapter will begin with the necessary inputs and parameters required to find the ground state structure through optimisation of the Kohn-Sham states. The latter parts will explore calculations of electronic and vibrational properties and how these are used to find the T_c of the material. Both will suggest any changes to default parameter values and some solutions to possible issues that may arise.

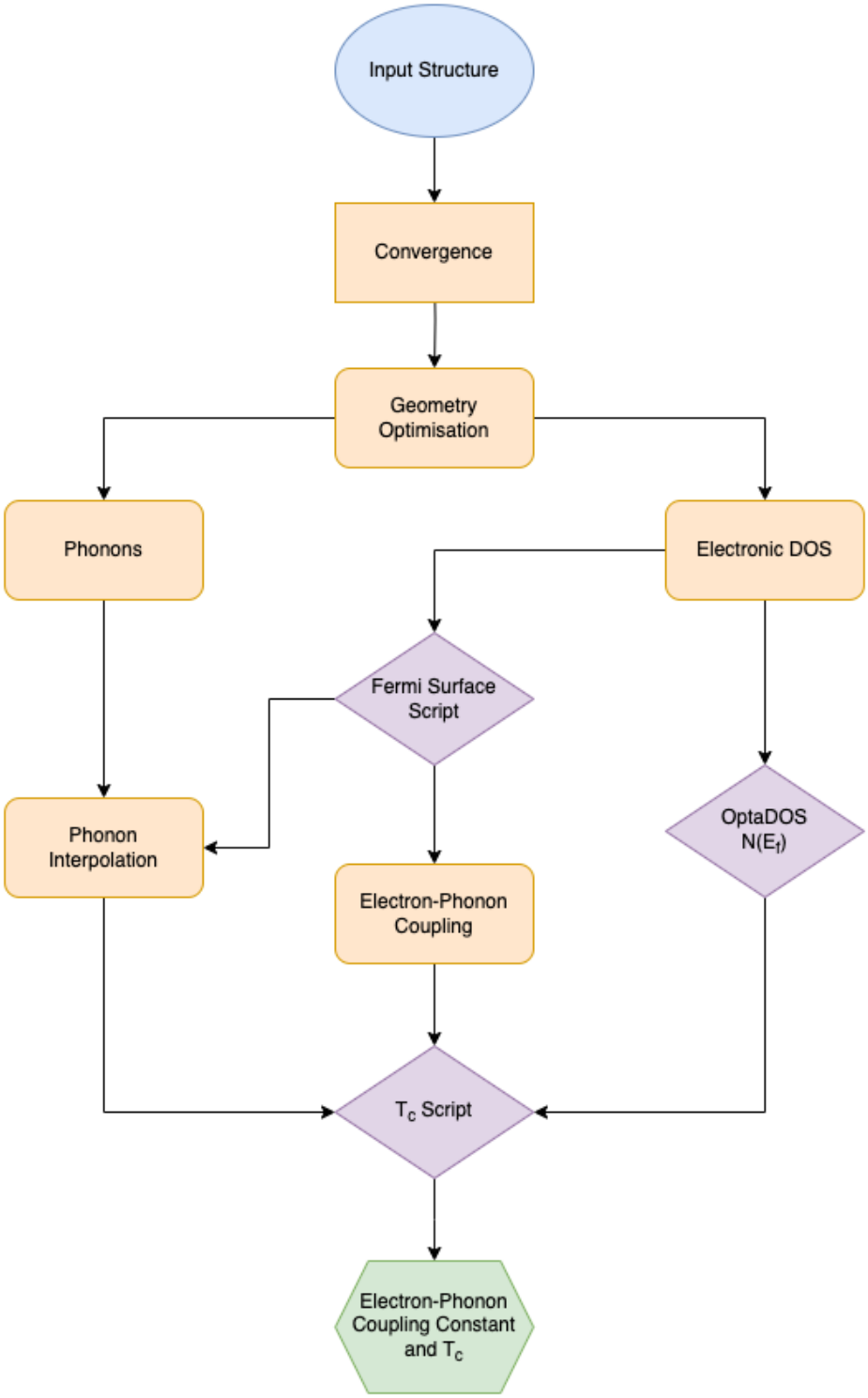

Figure 4.1: A flowchart showing the process used to find the T_c for a given input structure. Note that orange components relate to calculations completed using CASTEP, while purple components use personal or third-party scripts (as in the case of OptaDOS).[67]

4.2 Finding the Optimised Structure

Chapter 2 described two key input parameters required for CASTEP calculations – the k-point sampling and the cut-off energy. If computational cost were no issue, one could simply use an infinite cut-off energy and an infinite number of k-points to provide the most accurate description of the material. In reality, a careful balance must be found between computational cost and physical accuracy. Generally, the error in total energy per atom may be used to test convergence. The process in which this is calculated is summarised in Figure 4.2. Trial wavefunctions are generated, from which an initial density $n(r)$ is obtained. We can then construct a Hamiltonian within the Kohn-Sham scheme and solve the resultant Schrödinger equation to find the Kohn-Sham states and the associated energy. The change in energy can then be compared to the previously calculated energies and, if they are within a tolerable margin of error, may be taken as the ground state energy.

Regarding phonon calculations, however, it is much more useful to use maximum stress. Stresses will converge slower than total energy, giving more accurate results for parameters, demonstrated in Figure 4.3, and will provide greater accuracy in the structure. Hence, these two parameters are converged to within 0.1 GPa to maintain both accuracy and efficiency. The components of the stress tensor, σ_{ij} are

$$\sigma_{ij} = -\frac{1}{V}\frac{\partial E}{\partial \varepsilon_{ij}}, \tag{4.1}$$

where V is the unit cell volume. The components of the strain tensor, ε, are

$$\mathbf{h}' = (I + \varepsilon)\mathbf{h}, \tag{4.2}$$

where $\mathbf{h}$ consists of the unit cell vector columns a, b, c.

The convergence of the cut-off energy can be made quicker through the use of a finer fast Fourier transform (FFT) grid. The wavefunctions and densities calculated are stored on the grids, however, with $n(\mathbf{r}) = |\psi(r)|^2$, the density will contain G-vectors from 0 to $2G_{max}$. Therefore, we can store the density accurately on a finer grid. The FFT grid allows for the discretisation of real space in reciprocal space for more efficient calculations. The size of this grid must be large enough to accommodate every function within the plane wave basis set, such that $|G| \leq 2|G_{max}|$. If the grid is too small, aliasing errors may occur, in which higher frequency plane waves may be misrepresented. Generally, the grid size can be made smaller without a significant hindrance to accuracy, particularly when using LDA as the XC functional. For PBE and other GGA functionals, $1.75G_{max}$ to $2G_{max}$ is recommended. In these calculations, $2G_{max}$ is used to maintain consistent accuracy.

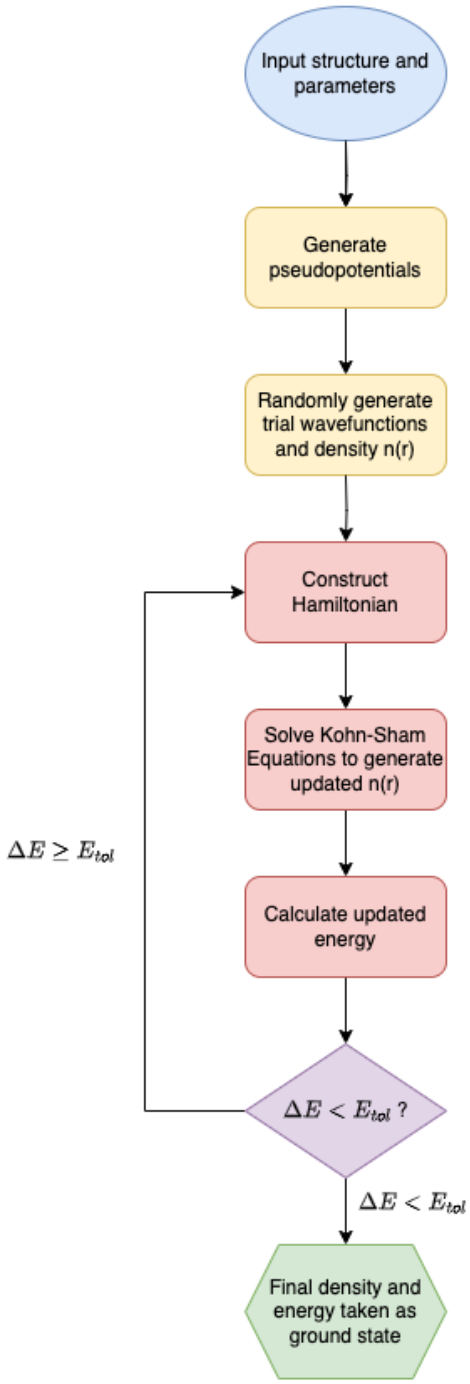

Figure 4.2: A flowchart summarising the process used to calculate the ground state energy using a self-consistent loop. E_{tol} is an adjustable parameter that determines the convergence tolerance between previous and current energies, set by `elec_energy_tol`.

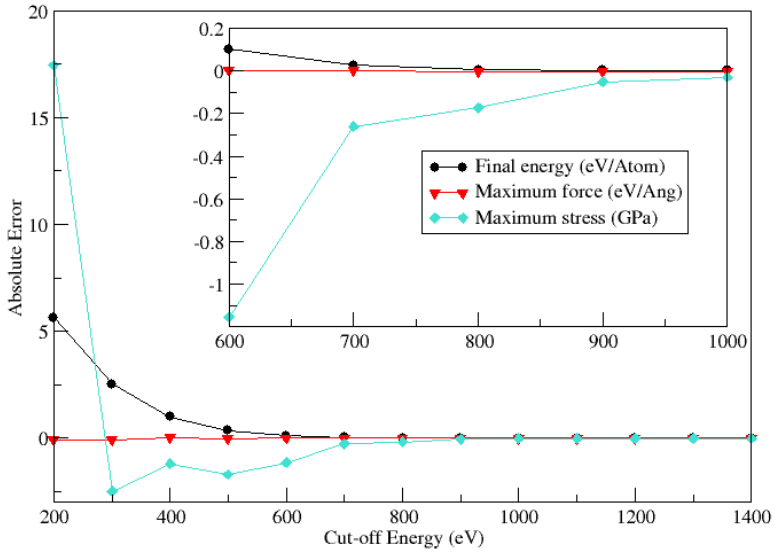

(a) Cut-off energy convergence using a k-point grid of $1 \times 1 \times 1$.

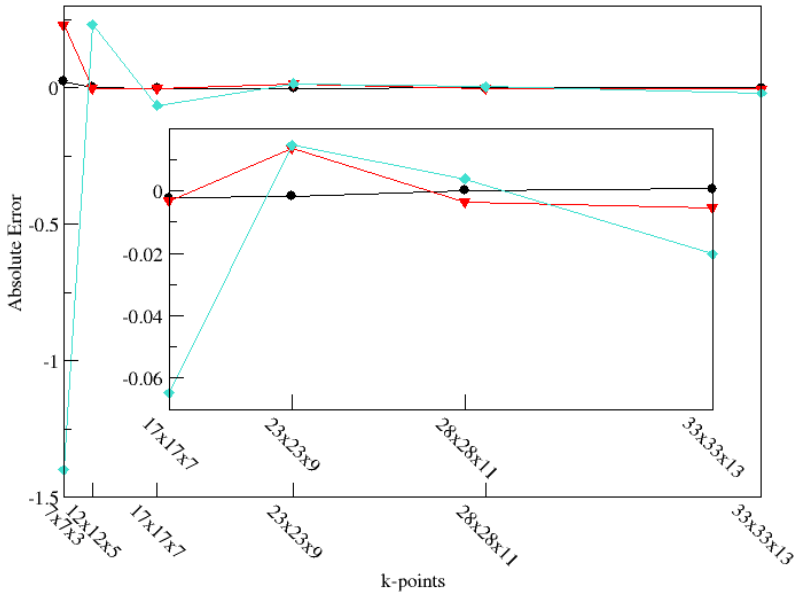

(b) K-point sampling convergence using a cut-off energy of 200 eV.

Figure 4.3: (a) Cut-off energy and (b) k-point sampling convergence graphs for the new material, $LiAlB_4$. In both cases, the total energy converges with smaller basis sets and k-point grids than the stress. The errors are calculated as the difference to the largest cut-off energy or set of k-points tested. Convergence carried out with CASTEPconv.

From the set of k-points given for a calculation, the total number of k-points required for calculations can be reduced using symmetry to an irreducible wedge within the BZ. This wedge can then be mapped across the BZ to give a uniform sampling. This allows for a considerable reduction in computational cost with no adverse affect to the resultant accuracy.

Once both parameters have been sufficiently converged, a geometry optimisation calculation [68] can be carried out to minimise the enthalpy of the structure with respect to the atomic positions. While there are a number of methods to find the minimum, the most common (and the default approach within CASTEP) is the limited-memory Broyden-Fletcher-Goldberg-Shanno (LBFGS) algorithm. The energy surface around a minimum is quadratic in small displacements and so is completely described by a Hessian matrix, **A**, consisting of the second derivatives of the energy:

$$\mathbf{A} = \begin{pmatrix} \frac{\partial^2 E}{\partial x_1 x_1} & \cdots & \frac{\partial^2 E}{\partial x_1 x_N} \\ \vdots & \ddots & \vdots \\ \frac{\partial^2 E}{\partial x_N x_1} & \cdots & \frac{\partial^2 E}{\partial x_N x_N} \end{pmatrix} \tag{4.3}$$

where x is some small displacement. If we knew **A**, the minimum could be found through

$$\delta E = \frac{1}{2}(\mathbf{X} - \mathbf{X}_{min})^T \cdot \mathbf{A} \cdot (\mathbf{X} - \mathbf{X}_{min}). \tag{4.4}$$

It can be seen that **A** is equivalent to the FCM, which, without a full phonon calculation, is unknown. Instead, an approximation to the inverse of **A** is iteratively built up as the positions of the ions are moved. The limited-memory algorithm does not store the full Hessian, but only a limited number of updates. It should be duly noted that while this minimisation process reliably finds the local minimum, this minimum may not be the global minimum for the material and, therefore, may be thermodynamically unstable in practice.

4.3 Electronic Properties

To understand more about the electronic properties of a material, it is helpful to consider how the energy of states varies across the BZ. Considering a particular wavefunction,

$$\psi(\mathbf{r}) = e^{i\mathbf{k}.\mathbf{r}} u(\mathbf{r}), \tag{4.5}$$

we can understand this variation using the limits of electrons with high potential energy and high kinetic energy respectively.

In the first case, neglecting kinetic energy gives very localised electrons, where we can consider the Hamiltonian operator to consist only of a contribution from the potential. We can then write the energy of the wavefunction as

$$\begin{aligned} E(\mathbf{k}) &= \int \psi^*(\mathbf{r}) V(\mathbf{r}) \psi(\mathbf{r}) d^3\mathbf{r} \\ &= \int V(\mathbf{r}) |e^{i\mathbf{k}.\mathbf{r}} u(\mathbf{r})|^2 d^3\mathbf{r} \\ &= \int V(\mathbf{r}) |u(\mathbf{r})|^2 d^3\mathbf{r}. \end{aligned} \tag{4.6}$$

The energy is invariant with respect to $\mathbf{k}$, thus, a simple flat band is produced.

In the second case, the Hamiltonian is now only given by the kinetic energy at the free electron limit:

$$\hat{H} = -\frac{1}{2m}\nabla^2 \tag{4.7}$$

As shown with Eq. (2.44), the wavefunction here can be expressed as

$$\psi(\mathbf{r}) = c_{\mathbf{Gk}} e^{i(\mathbf{k}+\mathbf{G}).\mathbf{r}}. \tag{4.8}$$

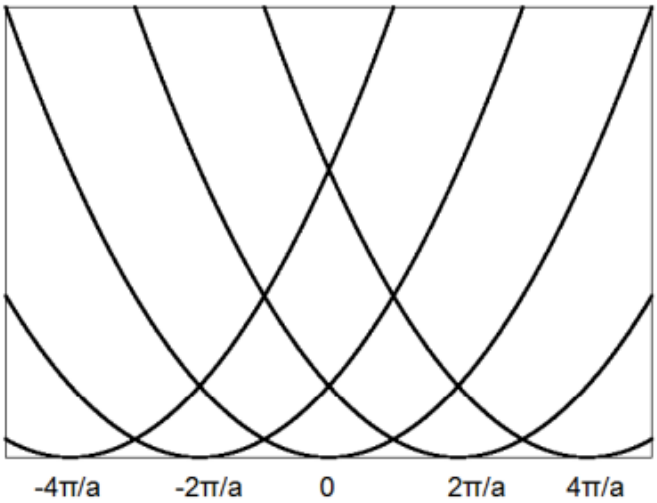

Figure 4.4: The band structure in the free electron limit. Due to the periodicity of states, the band structure can be reduced to the region bounded by $\frac{-\pi}{a}$ and $\frac{\pi}{a}$.[69]

The energy is therefore given by

$$\begin{aligned} E(\mathbf{k}) &= -\frac{1}{2m}\int \psi^*(\mathbf{r})\nabla^2\psi(\mathbf{r})d^3\mathbf{r} \\ &= \frac{1}{2m}(\mathbf{k}+\mathbf{G})^2\int \psi^*(\mathbf{r})\psi(\mathbf{r})d^3\mathbf{r} \\ &= \frac{1}{2m}(\mathbf{k}+\mathbf{G})^2. \end{aligned} \tag{4.9}$$

In this free electron limit then, the energy is quadratic with respect to $\mathbf{k}$, with a minimum at $\mathbf{k}+\mathbf{G}=0$. As these states are periodic in reciprocal space, this would give repeating parabolas about each lattice point (see Figure 4.4), which can be folded back to the first BZ.

4.4 Vibrational Properties

Ensuring well converged parameters to give an accurately energy-minimised structure is particularly important when proceeding to phonon calculations. As lattice dynamics works on the assumption that atoms in the cell are at their mechanical equilibrium, a high-precision geometry optimisation is crucial. Furthermore, it is necessary to satisfy the acoustic sum rule, for which the three lowest energy modes at the gamma point should be exactly zero, corresponding to the three translational symmetries for a period crystal. Poorly converged parameters may lead to insufficient sampling or numerical noise which breaks the sum rule.

The linear response method for DFPT employs a process similar to that of the ground state method. In this, a trial solution to the first-order wavefunctions in the Sternheimer equation is given, which is used to generate a first-order density. The Sternheimer equation is then solved to find a new set of wavefunctions, in turn giving a new first-order density. This repeats in a self-consistent loop until the density converges within a given tolerance. For this cycle to converge successfully, an accurate ground state energy surface is an important factor where, heuristically, the value for `elec_energy_tol` should be on the order of of `phonon_energy_tol`^{2}. As DFPT can calculate vibrational modes for $\mathbf{q}\neq 0$ as well as for $\mathbf{q}=0$, we can provide a set of q-points similarly to how we would for a set of k-points.

The computational cost of calculating modes for a single q-point is many times greater than for calculating the energy at a k-point. The issue of time to science is compounded by the fact that the use of symmetry between k-points in ground state calculations is not necessarily applicable to phonon calculations. Due to the vibrational movements of

the atoms within the BZ, the symmetry is often broken, requiring many q-points to be calculated on an individual basis. As such, it is recommended to use a smaller set of q-points, with a common practice being half the number of q-points in each dimension compared to **k**-points.

While this would generate a poor quality dispersion or density of states due to a lack of sampling, the hundreds or thousands of q-points required would be computationally intractable. Instead, using the dynamical matrices known for the coarse grid of wavevectors in the BZ, we can generate interatomic force constants for the FCM, along with the dynamical matrices and phonon frequencies for a finer set of q-points through Fourier interpolation.[70] The reverse Fourier transform of known dynamical matrices can be used to generate the FCM in real space. Another Fourier transform allows for approximations of the dynamical matrices at arbitrary q-points. This fine set of q-points is generally given as a grid for a density of states or along a path between points of high symmetry for a dispersion plot and can contain a high number of points due to the high speed at which interpolation occurs. When choosing this q-point set, it is important to contain the gamma point within the sampling points to enforce the acoustic sum rule. While grids with an odd number of q-points in each dimension will naturally contain the gamma point, we can shift an even grid of $p \times q \times r$ q-points to contain the gamma point using `phonon_fine_kpoint_mp_offset` $= \frac{1}{2p}\frac{1}{2q}\frac{1}{2r}$.

In this work, we also use a a set of wavevectors which link points on the Fermi surface. The interested reader should refer to Byrne's work for a more rigorous discussion of how these wavevectors are chosen. In essence, the band occupancy of a point within the BZ is compared with the occupancy of neighbouring points. If the maximum and minimum occupancies are not equal within a region, there must be a Fermi surface crossing, based on the intermediate value theorem.[37] Using the generated set of Fermi surface points, a set of phonon wavevectors are given by calculating $\mathbf{q}_{f,i} = \mathbf{k}_f - \mathbf{k}_i$ for each pair. The set of wavevectors can then be reduced by symmetry to give a representational set which link points across the entire Fermi surface.

4.5 Electron-Phonon Coupling

To calculate the electron-phonon matrix elements, we require the first-order potential as seen in Eq. (3.19). Taking analytic derivatives of the ground state pseudopotentials provides the first order contributions for the external nuclear potential. Contributions from the Hartree potential and the exchange and correlation potential are found through the Sternheimer equation as functionals of the first-order density. These contributions

arise from the interactions between the ground state and first-order densities. Once the perturbations have been calculated within the phonon calculations and interpolation, the matrix elements can be calculated by diagonalising the dynamical matrices and using the stored potentials.

As discussed in Chapter 3, these matrix elements can then be used within the Eliashberg spectral function to proceed with calculating the critical temperature of a material. In practice, this involves taking the `.epme` and `.phonon` files from the electron-phonon coupling and phonon interpolation calculations respectively, along with the density of states at the Fermi energy per unit cell. The DOS at E_f is given by an OptaDOS calculation using the `.bands` file from the CASTEP DOS calculation.

Chapter 5

Magnesium Diboride

5.1 Introduction

As discussed in Chapter 1, the key ingredient to the high T_c BCS superconductor that is MgB_2 lies with the strong electron-phonon coupling, in particular the contributions from the E_{2g} mode associated with vibrations of B atoms in the plane of the B sheets. It will also be interesting to evaluate the electron-phonon coupling strength, λ, as well as the choice of μ^* that provide a good fit to the experimental data. Electronic and vibrational properties will provide good insight into the accuracy of the results going forward, as there is a large amount of data to compare the results in this work against.

5.2 Method

The initial unit cell used was generated based on experimental data [71] to allow for convergence testing (see Figure 5.1) on the cut-off energy and k-point sampling. These were converged to within 0.1 GPa for the maximum stress, with the final energy converging to well within 0.01 eV/atom. A Monkhorst-Pack (MP) grid of $24 \times 24 \times 12$ k-points was used with a cut-off energy of 1200 eV and grid size of $2G_{max}$. The PBE exchange correlation functional was used for the convergence and all following calculations. The geometry optimisation process with the LBFGS method then relaxed the unit cell to find the lowest energy configuration of atomic positions. The tolerance for maximum stress was set to 0.1 GPa and a maximum force of 0.05 eV/Å.

Using the optimised structure, a band structure and electronic DOS calculation was carried out, including a PDOS. This used a finer k-point mesh of $72 \times 72 \times 36$. The DOS

at the Fermi energy per unit cell was measured within OptaDOS.[72, 73, 74] Using the resultant information on band locations within the BZ, the script described in the previous chapter was used to identify 10,000 points on the Fermi surface for phonon interpolation and 200 q-vectors linking points on the Fermi surface.

A DFPT calculation was made with a q-point grid of $12 \times 12 \times 6$, including an offset of $(\frac{1}{24}, \frac{1}{24}, \frac{1}{12})$ to ensure that the gamma point was included in the set of q-points, ensuring the acoustic sum rule is enforced. The phonon frequencies generated were interpolated across the 10,000 points identified on the Fermi surface to provide a smoother and more accurate phonon spectral function $F(\omega)$.

Following that, the electron-phonon coupling calculation was performed on the 200 identified q-vectors. The electron-phonon matrix elements were then used to find the spectral function $\alpha^2 F(\omega)$ across the range of phonon frequencies. This is achieved by first calculating for it directly, albeit coarsely, then using the phonon interpolation across the Fermi surface points for a finer result. Finally, this was fed into the Allen-Dynes equation across a range of values of μ^* to find an optimal value when comparing the Allen-Dynes T_c to the experimental value.

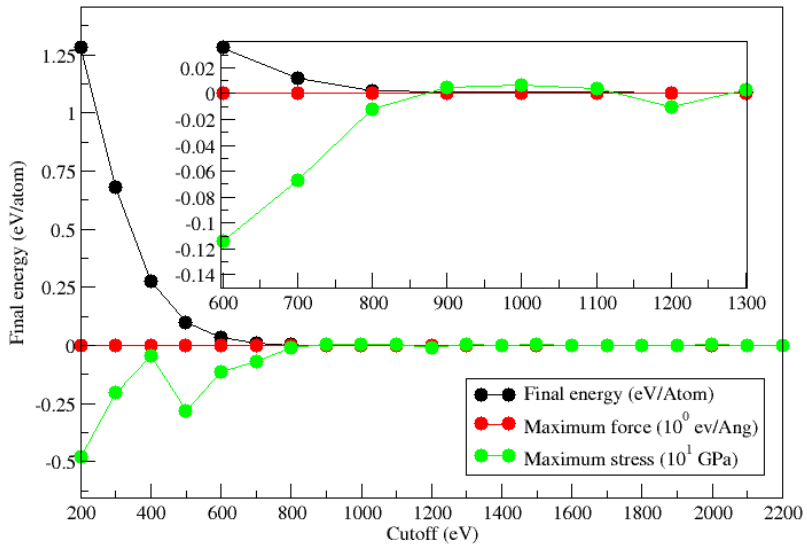

(a) Cut-off energy convergence using a k-point grid of $1 \times 1 \times 1$.

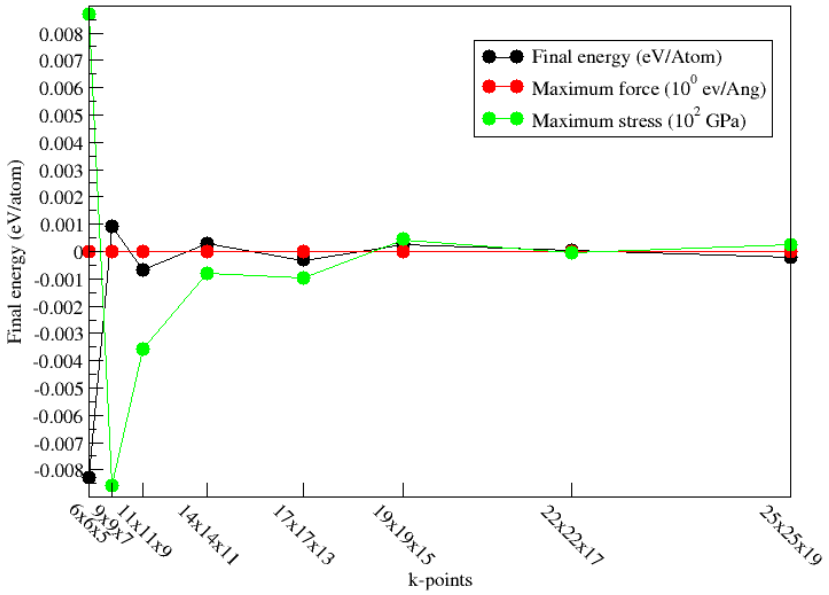

(b) K-point sampling convergence using a cut-off energy of 200 eV.

Figure 5.1: (a) Cut-off energy and (b) k-point sampling convergence graphs for magnesium diboride. The errors are calculated as the difference to the largest cut-off energy or set of k-points tested. Note that the k-point grid chosen was $24 \times 24 \times 12$ to provide simple factors with which to construct the phonon q-point grid, allowing for greater efficiency on phonon calculations. Convergence carried out with CASTEPconv.

5.3 Results and Discussion

5.3.1 Structure

In its hexagonal unit cell, the lattice parameters a and b refer to in-plane lengths which are equal here, while c gives the length orthogonal to the planes of the magnesium and boron sheets. While MgB_2 is a layered compound, the interlayer separation is relatively small. The bonding between layers has been previously acknowledged as a result of ionic charge transfer rather than van der Waal's forces.[75]

This is demonstrated in Table 5.1, where the use of semi-empirical dispersion corrections (SEDC) in the Tkatchenko-Schleffer scheme [76] is applied. It is clear that the use of LDA or SEDC leads to an overbinding effect between layers, giving a much smaller interlayer separation than in experimental data.

The interlayer separation of the calculated structure is very similar to the experimental data found in the literature, however, the in-plane lattice parameter shows overbinding from this work as well as in other computational works. This leads to a compression in the B-B bonds, which is known to slightly decrease the T_c due to both a reduction in $N(E_f)$ and an increase in the E_{2g} phonon frequency.

MgB_2	a (Å)	c (Å)
PBE (calc.)	3.073	3.522
PBE+SEDC (calc.)	3.031	3.435
PBE (lit.)	3.077	3.509
LDA (lit.)	3.036	3.436
Exp. (lit.)	3.085	3.521

Table 5.1: The relaxed structure of MgB_2 using PBE with and without SEDC compared to experimental results [77] and computational results which used both PBE and LDA.[78]

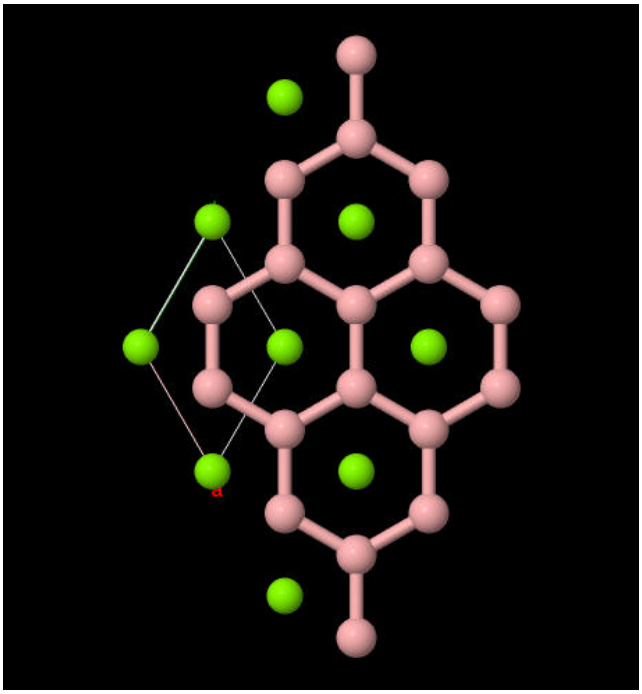

(a) Magnesium diboride as seen through the *c* axis.

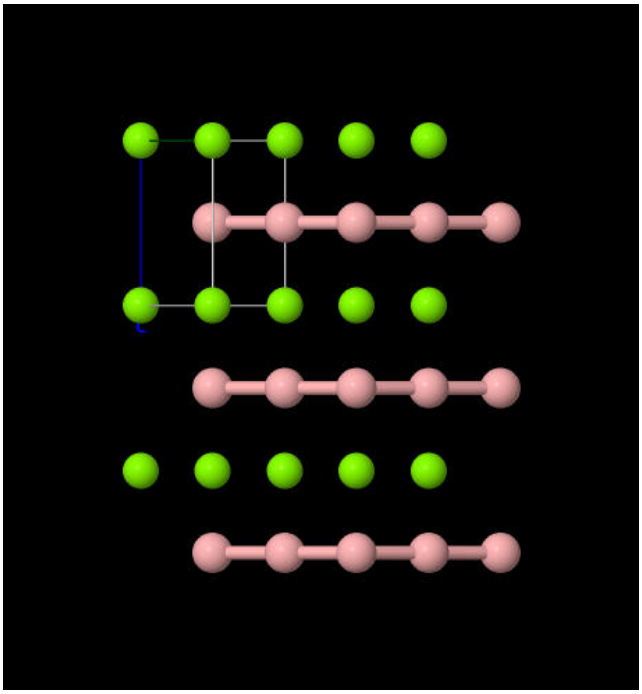

(b) Magnesium diboride as seen through the *ab* plane.

Figure 5.2: The relaxed structure of MgB_2 following a geometry optimisation, with alternating layers of honeycomb-structured boron (pink) and hexagonal magnesium (green). Each Mg atom is centred between the 6-membered boron rings above and below. Covalent bonds (pink) between B atoms have also been visualised.

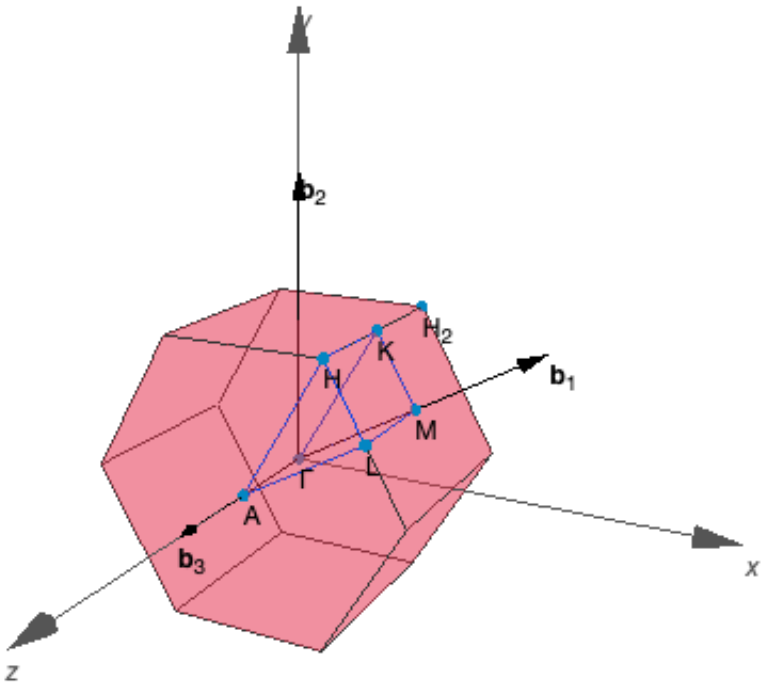

Figure 5.3: The first Brillouin zone for MgB_2 with points of high symmetry labelled. These points will later be used for creating phonon dispersion plots through interpolation. Diagram generated by SeeK-path using the CASTEP `.cell` file.[79, 80]

5.3.2 Electronic Properties

A Mulliken charge analysis of MgB_2, shown below in Table 5.2, further demonstrates the presence of ionic bonding between Mg and B, where Mg donates electron density to the *p*-orbitals of the boron sheets. The boron *s*-orbitals are meanwhile involved in covalent bonding to form the honeycomb structure.

Ion	s	p	Total	Charge (e)
B_1	1.00	2.67	3.67	-0.67
B_2	1.00	2.67	3.67	-0.67
Mg_1	0.15	0.51	0.66	+1.34

Table 5.2: A Mulliken charge analysis for each ion in the magnesium diboride primitive cell, indicating charge transfer from magnesium to boron *p*-orbitals.

Using OptaDOS with a sampling interval of 0.01 eV, the DOS at the Fermi energy was calculated as $N(E_f) = 0.7041$. Similarly to graphite, boron forms hybridised sp^2-orbitals in MgB_2, giving rise to the in-plane σ-band. Figure 5.4a displays the projected DOS (PDOS) for MgB_2, where the boron *p*-orbitals contribute most significantly to $N(E_f)$, with very little contribution from the *s*-orbitals. The majority of the contributions to the DOS

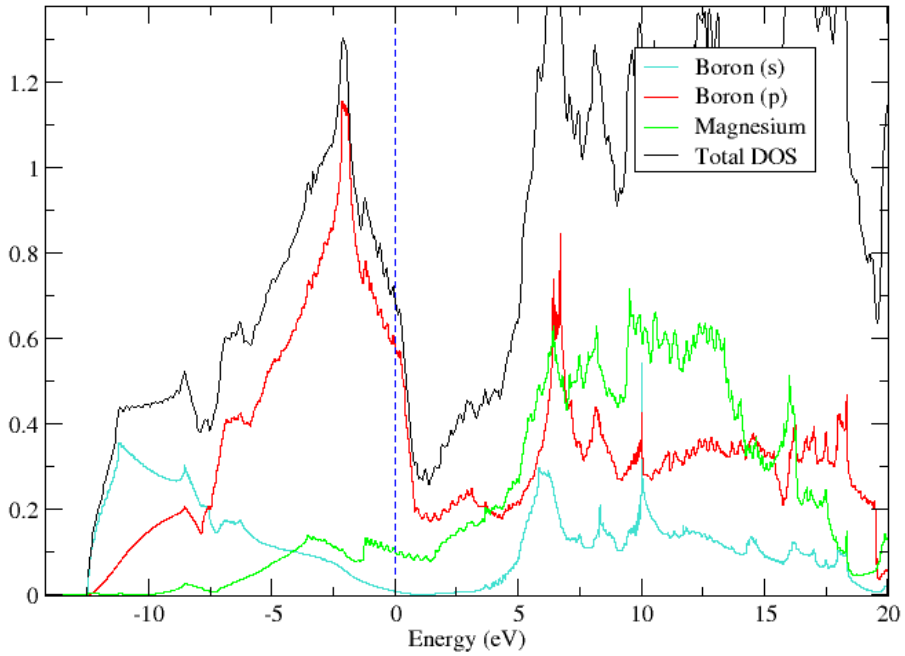

(a) The projected density of states (PDOS) of MgB_2.

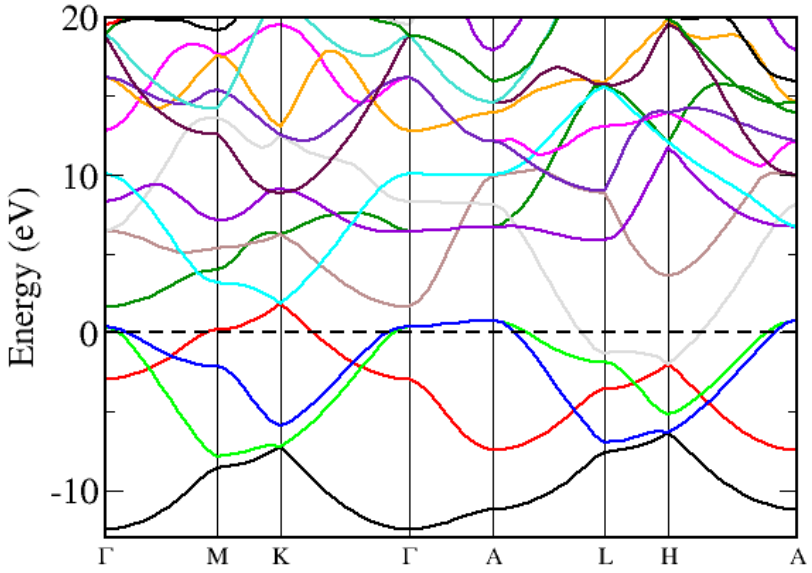

(b) The electronic band structure of MgB_2.

Figure 5.4: (a) The projected density of states (PDOS) and (b) electronic band structure for MgB_2. An initial DOS calculation on a fine k-point grid of $72 \times 72 \times 36$ was followed by (a) OptaDOS calculations at a sampling interval of 0.01 eV and (b) an interpolation using the symmetry points in the x-axis. The energies have been shifted to $E_f = 0$, with the Fermi energy represented by dashed lines.

from Mg come at higher energies. The band structure (Figure 5.4b) provides evidence of the metallic nature of MgB_2 through the absence of a band gap. The doubly degenerate flat band close to the Fermi level in the $\Gamma - A$ direction contributes significantly to $N(E_f)$ and can be attributed to $p_{x,y}$ orbitals which form the in-plane σ-band.

5.3.3 Phonon Properties

The vibrational properties for MgB_2 are summarised in Figure 5.5. The low frequency density of states increases quadratically from zero (indicating that the acoustic sum rule has been satisfied) due to the linearity of the band frequencies with respect to the gamma point.

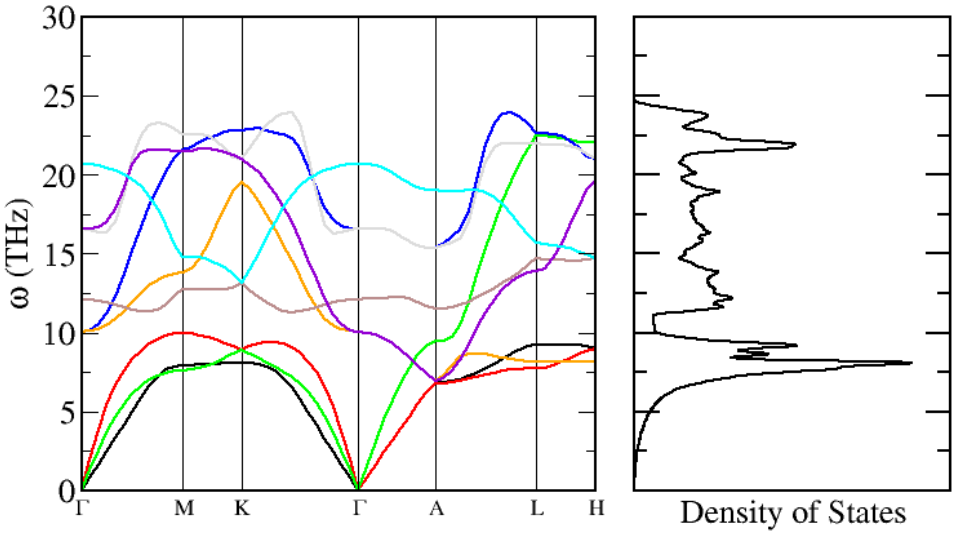

Figure 5.5: A dispersion (left) and DOS (right) plot for MgB_2. The lattice points on the x-axis were used as interpolation points for the dispersion plot, while a $48 \times 48 \times 24$ fine q-point grid (offset to include the Γ-point) was used for the DOS plot.

As seen in Figure 5.6, the largest peak in the phonon density of states is a result of modes associated with the Mg atoms at a low frequency, around 7.5 THz. The higher frequency range beyond the dip centred at 10.5 THz is built on modes associated with the boron atoms, including the E_{2g} mode which is known to contribute significantly to the electron-phonon coupling strength.

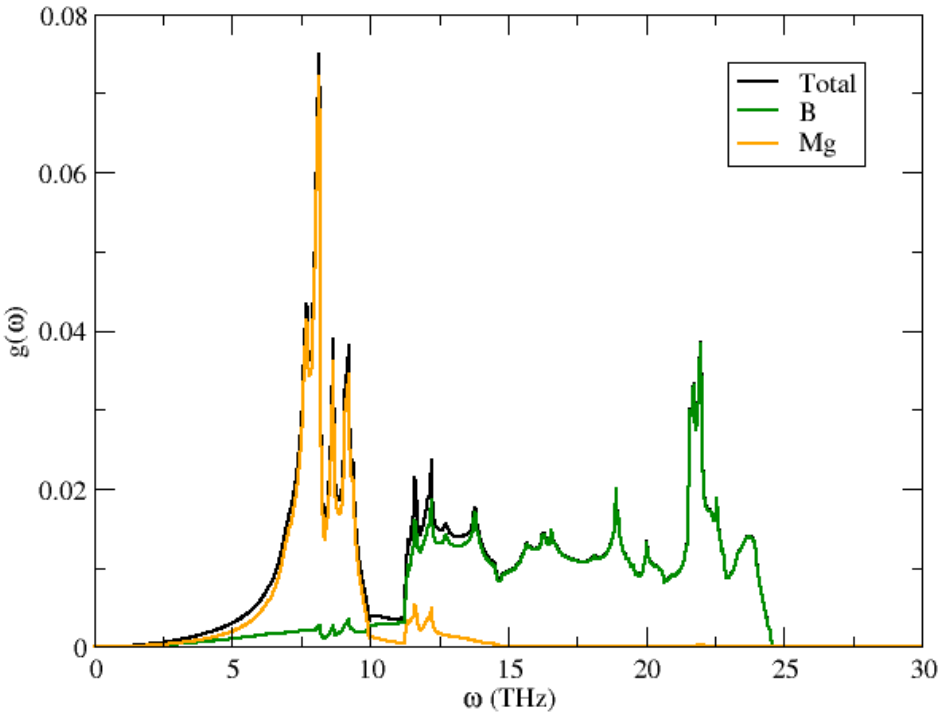

Figure 5.6: An element-resolved phonon DOS for MgB_2. It can be seen that lower frequency phonon modes are related to vibrations predominantly involving Mg atoms, while higher frequency modes are associated with B atoms.

5.3.4 Electron-Phonon Coupling and Superconductivity

The high-frequency boron-associated phonon modes at around 16 THz and 22 THz are seen to contribute greatly to the Eliashberg spectral function (see Figure 5.7), with the former being the E_{2g} mode. At a lower frequency, with a large degree of electron-phonon coupling, this in-plane boron vibration generates a significant contribution to the electron-phonon coupling strength, λ.

The value of λ itself varies significantly within the first principles literature, largely due to the two-gap nature of MgB_2 often producing a case each for weak coupling and moderate to strong coupling. These derive from the two Fermi surfaces MgB_2 produces from its π- and σ-band networks respectively (see Figure 1.1b) and generally give an effective coupling constant of $0.7 < \lambda_{eff} < 1.0$. Here, we find $\lambda = 1.011$, falling within the range found by Margine and Giustino [81] for the coupling to σ sheets. This is also similar to recent experimental findings, which, dependent on fabrication method, find $\lambda \approx 1.094$.[82]

To find a reasonable value of μ^* to input for calculations with $LiAlB_4$, a range of values were tested for MgB_2, from 0.10 – 0.16 at intervals of 0.01 (see Figure 5.8). A good level of agreement with experimental values was achieved with $\mu^* = 0.10$, which, through the Allen-Dynes formula, gives $T_c = 39.16$ K. This chosen value of μ^* is consistent with the reasonable range of values found to be used in the literature.

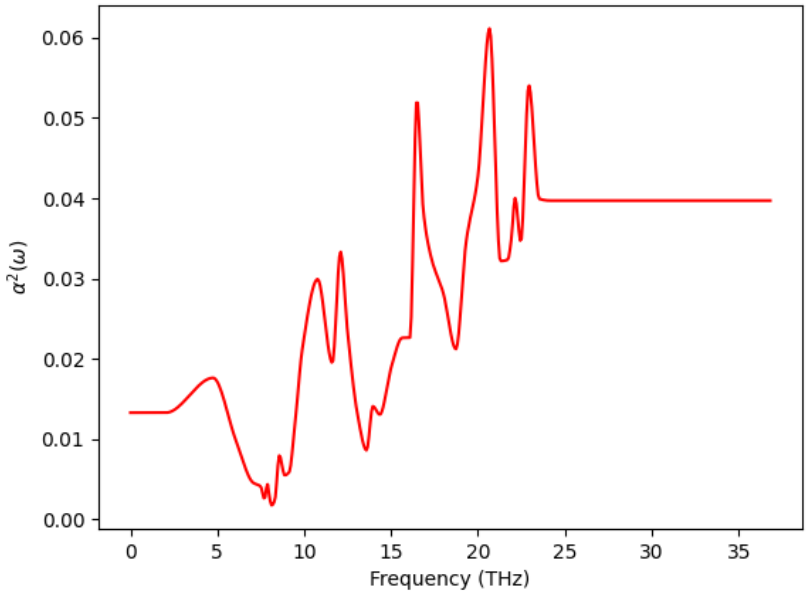

(a) $\alpha^2(\omega)$ function against phonon frequency, ω.

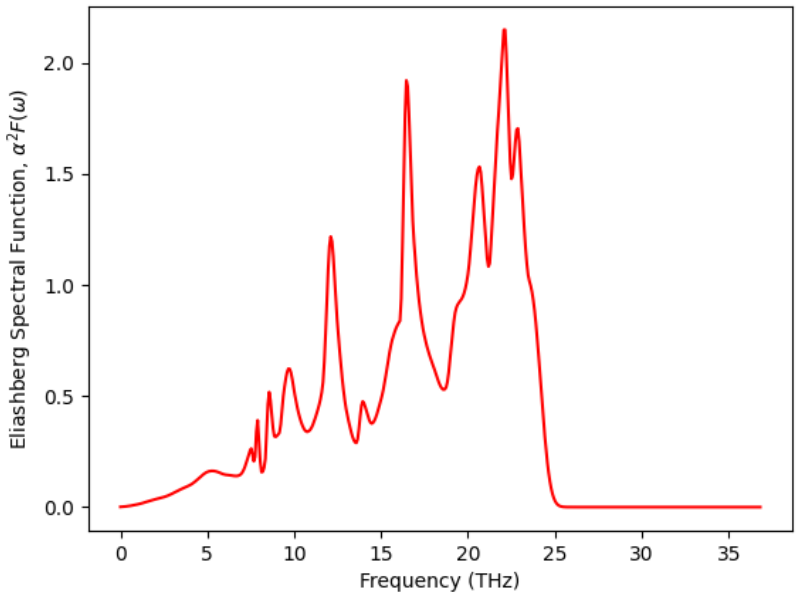

(b) $\alpha^2F(\omega)$ function against phonon frequency, ω.

Figure 5.7: (a) The electron-phonon coupling function and (b) the Eliashberg spectral function for MgB_2, indicating the contributions of phonon modes to the electron-phonon interaction induced superconductivity.

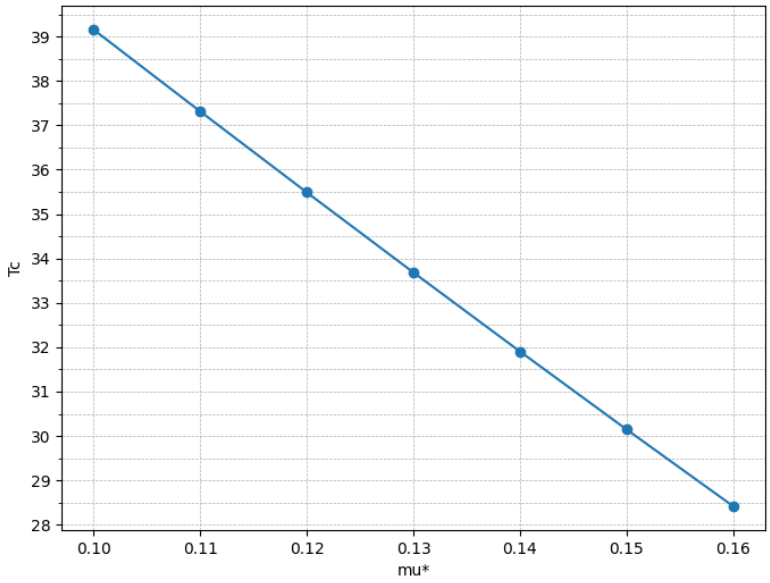

Figure 5.8: The change in T_c depending on the choice of μ^* for MgB_2. $\mu^* = 0.1$ provides a T_c in excellent agreement to experimental results, for which $T_c = 39$ K.[1]

5.4 Conclusions

The calculated structural, electronic, and phonon properties generally demonstrate good agreement with expectations from the literature, notably a clearly predominant contribution of B orbitals to $N(E_f)$ and a significant contribution of the E_{2g} phonon mode to the overall electron-phonon coupling constant. This culminates in an accurate critical temperature whilst maintaining a reasonable value for μ^*, which can be taken as a loose fitting parameter for further calculations on similar structures.

Nevertheless, it is difficult to maintain high levels of certainty without further testing. Potential sources of error include the choice of functional, the reduced B-B bond lengths and, the most significant of error contributions, the uncertainty of μ^*, which itself gives $28.42 \leq T_c \leq 39.16$ for $0.1 \leq \mu^* \leq 0.16$. As such, the result yields an attractive T_c but requires further verification in time.

Chapter 6

$LiAlB_4$

6.1 Introduction

Focusing the search on layered materials with a similar structure to MgB_2, we find a group of boron-based layered materials, introduced by Tayran et al.[83] and suggested by Hao et al. for applications in metal-ion batteries.[84] In contrast to MgB_2, the structure suggested was based on the layered structure of $YCrB_4$, involving B sheets consisting of 5- and 7-membered rings rather than the 6-membered rings in MgB_2, alternating with metal layers composed of two different elements as seen in Figure 6.1.

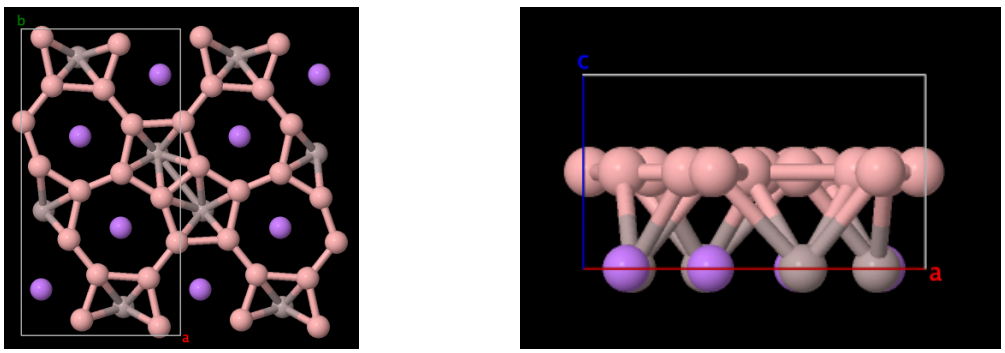

(a) $YCrB_4$-type $LiAlB_4$ as seen through the *c* axis.

(b) $YCrB_4$-type $LiAlB_4$ as seen through the *ab* plane.

Figure 6.1: The relaxed structure of $YCrB_4$-analogous $LiAlB_4$ following a geometry optimisation. The structure consists of alternating layers of B (pink) and mixed Li (purple) and Al (grey), where the B sheets consist of 5- and 7-membered rings.

Tayran et al. found that, for the $YCrB_4$-type $XAlB_4$ structures (M = Mg, Li, Na, Ca), the Mg-, Ca- and Li-based aluminium tetraborates were thermodynamically stable,

whereas $NaAlB_4$ was not. Furthermore, all compounds were found to be dynamically stable. Drawing similarity to $MgAlB_4$, a known superconductor ($T_c \approx 12$ K), we look at X = Li, Ca, Na, Be, as well as considering $MgAlB_2C_2$ to simulate carbon-doping similarly to that which has been tested for MgB_2.[82] While also involving two metal elements as the $YCrB_4$-type structures do, the known structure for $MgAlB_4$ consists of separated alternating metal layers rather than mixed metal layers. Given the similarity of the set of tested compounds to $MgAlB_4$, the $XAlB_4$ structures all consist of input unit cells with pure metal layers, repeating with boron in a pattern of X-B-Al-B.

The formation enthalpies of the $XAlB_4$ compounds suggested by Tayran are calculated in both the $YCrB_4$-type structure and an MgB_2-type structure based on the structure of $MgAlB_4$. The formation enthalpy is given by

$$H_f^{XAlB_4} = H_{atom}^X + H_{atom}^{Al} + 4H_{atom}^B, \tag{6.1}$$

where H_{atom} for each element is the enthalpy obtained from their ground state crystalline structure per atom. The thermodynamic stability can then be evaluated with ΔH, which is simply

$$\Delta H = H_{gs}^{XAlB_4} - H_f^{XAlB_4}, \tag{6.2}$$

where $H_{gs}^{XAlB_4}$ is the ground state enthalpy calculated from a converged geometry optimisation calculation for the compound. The results are summarised below in Table 6.1.

		Enthalpy (eV/cell)	
Compound	Formation Enthalpy	MgB_2-type (ΔH)	$YCrB_4$-type (ΔH)
$MgAlB_4$	-695.07	-695.88 (-0.81)	-695.57 (-0.50)
$LiAlB_4$	-755.24	-755.97 (-0.73)	-755.55 (-0.31)
$CaAlB_4$	-1567.29	-1568.21 (-0.92)	-1569.03 (-1.74)
$NaAlB_4$	-1790.91	-1789.75 (+1.15)	-1790.42 (+0.49)
$BeAlB_4$	-939.99	-939.91 (+0.09)	
$MgAlB_2C_2$	-837.03	-836.47 (+0.55)	

Table 6.1: The formation enthalpies for studied compounds, with those suggested by Tayran calculated for both the MgB_2- and $YCrB_4$-type structures. Values in brackets pertain to the difference between the formation enthalpy calculated and the ground state enthalpy for the compound.

By testing the MgB_2-type enthalpies against the $YCrB_4$-type enthalpies, we provide a slightly greater security of thermodynamic stability than only the formation enthalpy by comparing to similar structures which have been studied. Corroborating with Tayran et al.'s work, we find that the $YCrB_4$-type structures excluding $NaAlB_4$ are thermodynamically stable. However, compounds incorporating Mg are more stable in the MgB_2 configuration

as expected, while this is also the case for Li-incorporated structures. Conversely, $CaAlB_4$ is more stable with 5- and 7-membered rings and, as such, will not be included going forward. Of the structures not included in Tayran's work, $BeAlB_4$ has $\Delta H = +0.09$, or +0.015 eV/atom, while $MgAlB_2C_2$ was found to be significantly less stable than its constituent elements, as well as $MgAlB_4$ without carbon-doping. As this is reasonably close to stability, further study was carried out to calculate the phonon modes for the compound. This demonstrated a lack of dynamic stability as well, due to the presence of imaginary phonons, suggesting that applied forces would yield a structure of greater stability than the input layered structure. In both cases of $BeAlB_4$ and $MgAlB_2C_2$, the $YCrB_4$-type structures were not studied, given that the MgB_2-type structures were already found to be unstable through formation enthalpies.

Therefore, the focus for the remainder of the chapter will remain with the new structure, $LiAlB_4$, with the boron sheets arranged in the 6-membered ring configuration with the aim of replicating the success of the MgB_2 E_{2g} phonon.

6.2 Method

The initial input unit cell was derived from the structure of $MgAlB_4$, replacing Mg with Li. The PBE functional was again used for all calculations in CASTEP. Through convergence testing (see Figure 4.3), a cut-off energy of 900 eV and grid size of $2G_{max}$ was chosen, along with a k-point MP grid of $27 \times 27 \times 12$, allowing for a simple choice for the phonon q-point grid for the later phonon calculations. The converged parameters were within a tolerance of 0.05 GPa for the maximum stress and within a 0.01 eV tolerance for the energy. A geometry optimisation with a tolerance for maximum stress set to 0.1 GPa and a maximum force of 0.05 eV/Å gave the energy-minimised structure.

The electronic properties were calculated with a fine grid of $54 \times 54 \times 24$, again using OptaDOS for the computation of $N(E_f)$. Using the information on the band structure and Fermi surface, 10,000 points on the Fermi surface were chosen for phonon interpolation, with 243 q-vectors connecting Fermi surface points.

The vibrational calculations were performed on a q-point MP grid of $9 \times 9 \times 4$. Following the interpolation across the 10,000 Fermi surface points, an electron-phonon coupling calculation on the 243 chosen q-vectors was carried out. For the calculation of the T_c, $\mu^* = 0.1$ was considered as the most likely value from fitting this parameter in the MgB_2 calculation, however, a range of μ^* values were still used as there is no guarantee that this would be equivalent for the two structures, despite their similarities.

6.3 Results and Discussion

6.3.1 Structure

The structure of $LiAlB_4$ closely resembles that of MgB_2, though the metal layers now alternate between hexagonal layers of Li and Al. The lattice parameters here are $a = 3.00$Å and $c = 6.71$Å. Considering that the number of layers per unit cell is doubled compared to that of MgB_2, we find an average interlayer separation of approximately 1.678Å compared to 1.761Å for MgB_2. The Li-B separation is 1.779Å, while the Al-B separation is 1.575Å, indicating stronger Al-B bonding, given that Li has a much smaller ionic radius than Al. Generally, a compression along the c axis leads to a reduced T_c within MgB_2, attributed to an increase in the E_{2g} phonon frequency.

Similarly to the case of MgB_2, the application of SEDC with the PBE functional leads to a 5% decrease in c. The interlayer separation is already suggestive of an ionic bonding system between metal and boron layers rather than through van der Waal's forces.

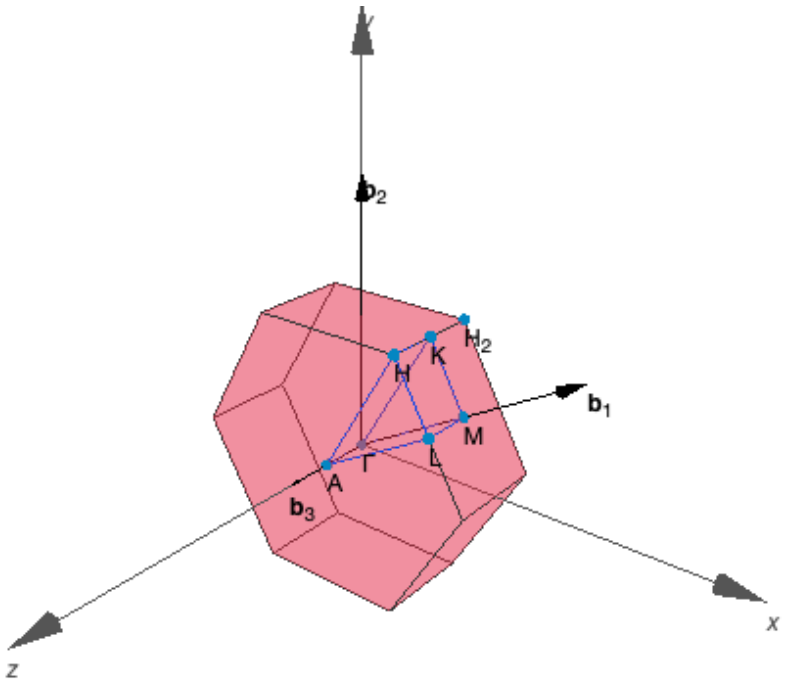

Figure 6.2: The first Brillouin zone for $LiAlB_4$. The BZ for $LiAlB_4$ is shorter in the z-direction due to a larger real-space cell in this direction than MgB_2. Diagram generated by SeeK-path.

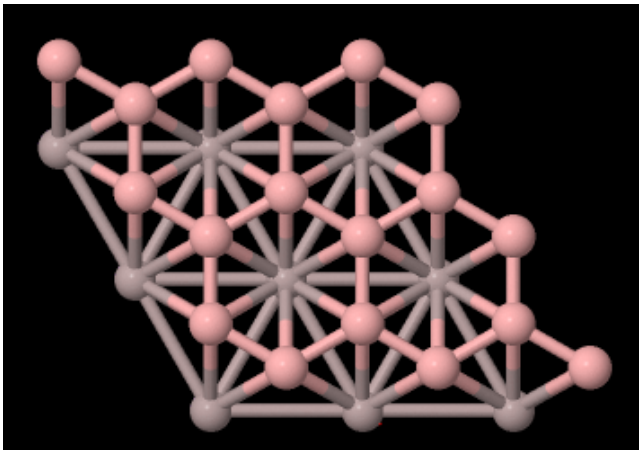

(a) $LiAlB_4$ as seen through the *c* axis.

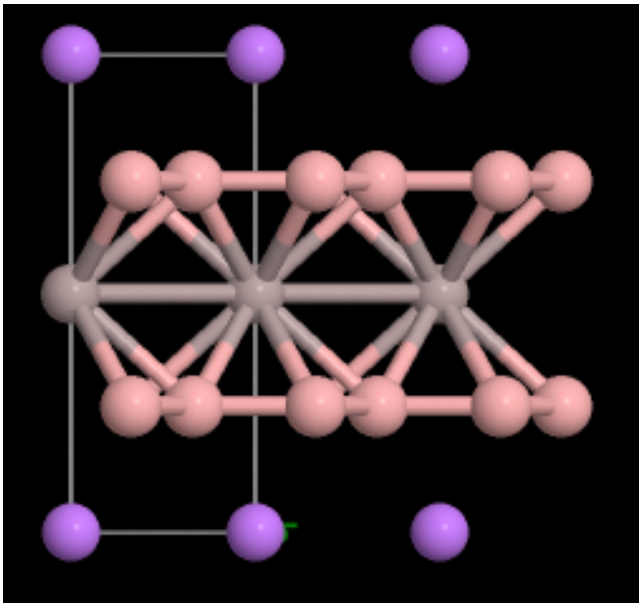

(b) $LiAlB_4$ as seen through the *ab* plane.

Figure 6.3: The relaxed structure of $LiAlB_4$ following a geometry optimisation. The structure consists of alternating layers of Li (purple), Al (grey), and B (pink).

6.3.2 Electronic Properties

A Mulliken charge analysis (see Table 6.2) demonstrates the ionic nature of the system, with both Li and Al donating electron density to the boron p-orbitals. A stronger charge on the Al ion of +1.28 compared to +1.04 for Li corroborates with the structural findings to suggest that Al bonds more strongly with B than Li. Similarly to MgB_2, $LiAlB_4$ maintains the boron sheet's honeycomb structure through σ-band covalent bonds, with the π-band contributing to interlayer stability.

Ion	s	p	Total	Charge (e)
Li_1	1.57	0.39	1.96	+1.04
B_1	0.94	2.64	3.58	-0.58
B_2	0.94	2.64	3.58	-0.58
B_3	0.94	2.64	3.58	-0.58
B_4	0.94	2.64	3.58	-0.58
Al_1	0.53	1.19	1.72	+1.28

Table 6.2: A Mulliken charge analysis for each ion in the $LiAlB_4$ primitive cell.

Through OptaDOS, we find $N(E_f) = 1.33$ for a sampling interval of 0.01 eV. Given that the $LiAlB_4$ unit cell contains twice as many ions as the MgB_2 unit cell, these can be compared by halving the calculated $N(E_f)$ for $LiAlB_4$ to 0.65, a 7.7% decrease from MgB_2. The PDOS (see Figure 6.4a) displays clear similarities with that of MgB_2, most notably at $N(E_f)$, for which the boron p-orbitals contribute most significantly. Furthermore, the contributions from both metals to the DOS are largely situated at energies much higher than E_f and the lack of a band gap (see Figure 6.4b) demonstrates the metallic nature of $LiAlB_4$. The low energy states in the PDOS for boron s-orbitals and Al behave as step functions, relating to highly localised core states. The presence of two doubly degenerate flat bands close to the Fermi level in the $\Gamma - A$ direction contribute significantly to $N(E_f)$. Similarly to MgB_2, these flat bands relate to boron $p_{x,y}$ orbitals which form the σ-bands in each boron sheet. With a peak in the DOS at approximately -2.7 eV from E_f, the use of p-type doping would provide a favourable shift in $N(E_f)$. However, there has been significant difficulty in successfully synthesising hole-doped MgB_2, with a successful Cu-doped sample achieving a lower T_c regardless.[85] As such, hole-doping $LiAlB_4$ is likely to present similar issues, but should be investigated in the future.

As a means to approximate the effect of pressure on the critical temperature, we also examine $N(E_f)$ under hydrostatic pressure and biaxial strain, summarised in Table 6.3. The strain in each axis is estimated by the percentage change in a given lattice parameter from those calculated without external pressure.

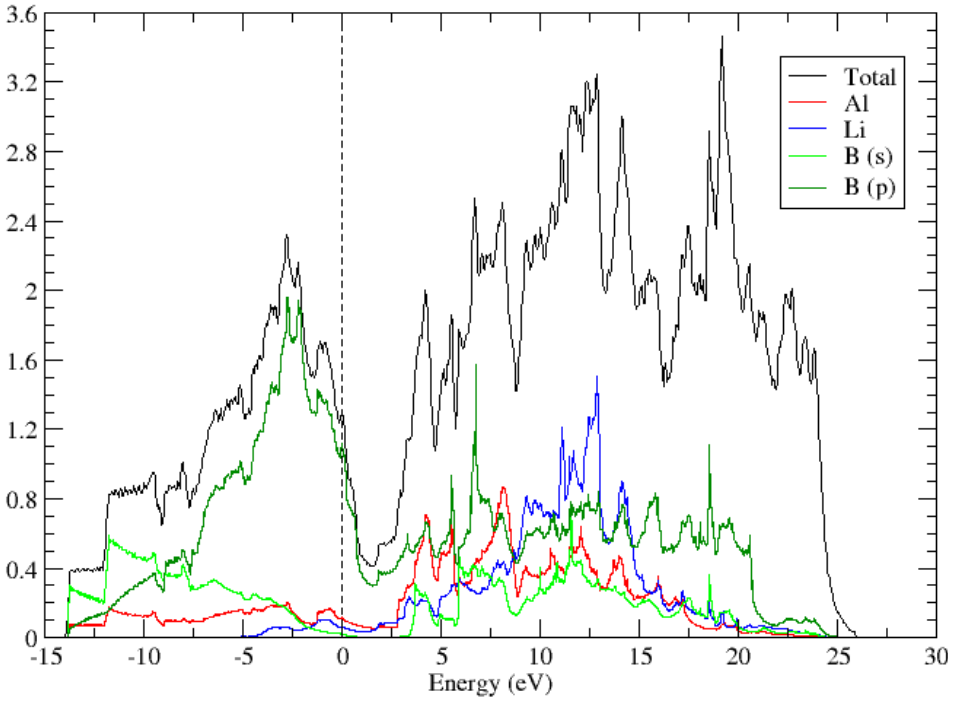

(a) The electronic PDOS of $LiAlB_4$.

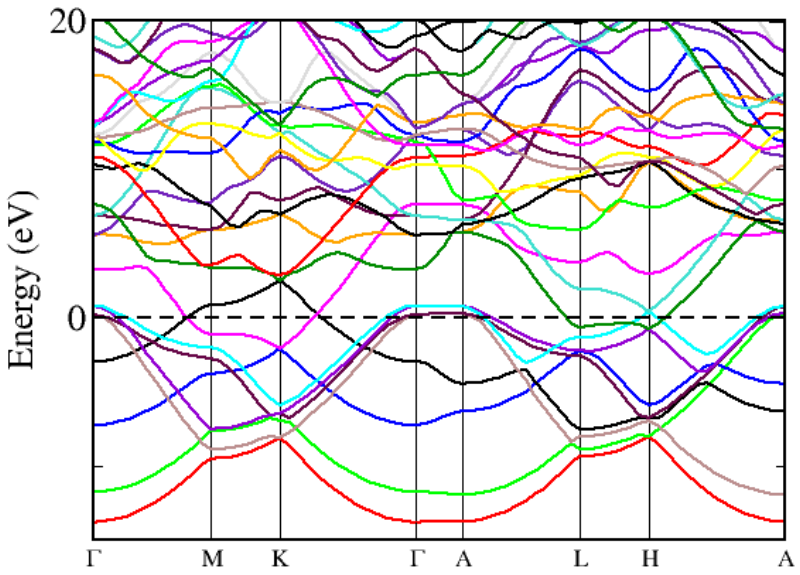

(b) The electronic band structure of $LiAlB_4$.

Figure 6.4: (a) The PDOS and (b) electronic band structure for $LiAlB_4$. An initial DOS calculation on a fine k-point grid of $54 \times 54 \times 24$ was followed by (a) OptaDOS calculations at a sampling interval of 0.01 eV and (b) an interpolation using the symmetry points in the x-axis. The energies have been shifted to $E_f = 0$, with the Fermi energy represented by dashed lines.

Pressure (GPa)	Type (axis)	$N(E_f)$	Strain in a (%)	Strain in c %
0	–	1.33	0	0
+100	Isotropic	0.726	-6.59	-25.2
-100	Isotropic	1.39	+9.76	9.86
+50	Biaxial (ab)	1.1372	-6.86	+1.55
+50	Uniaxial (c)	0.7849	+2.61	-22.8

Table 6.3: The change in the density of states at the Fermi energy dependent on different pressures. The strain through lattice parameters a and c are given as percentage changes.

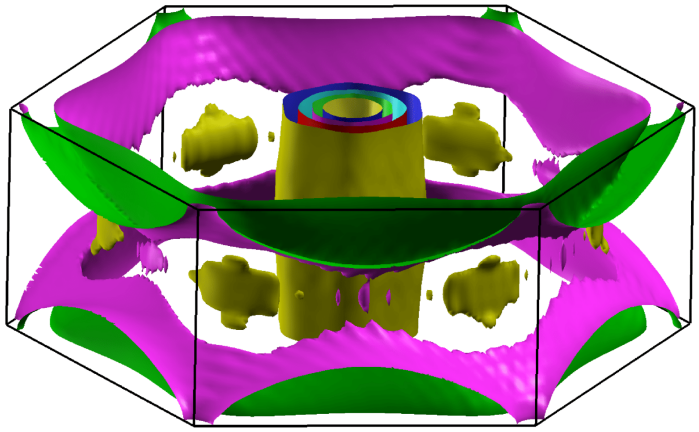

Figure 6.5: The Fermi surface of $LiAlB_4$, generated by Ertugrul Karaca. Similarly to MgB_2, we find separated sheets, now with the cylindrical sheet central to the BZ.

For these calculations, the tolerances for the geometry optimisation were set to a coarser convergence tolerance to facilitate their investigation, with only the biaxial pressure satisfying the usual tolerance. The failure to converge with isotropic and uniaxial pressures indicates a degree of structural instability caused by these pressures. Here we find similar results to that of the known pressure-dependence of the T_c for MgB_2. Isotropic pressure on $LiAlB_4$ leads to a decrease in $N(E_f)$, while negative pressures lead to a slight increase. Similarly, biaxial compression causes an expected decrease in $N(E_f)$, while uniaxial compression leads to a significant reduction, demonstrating that the interlayer separation is crucial to $N(E_f)$ and, by extension, the critical temperature.

6.3.3 Phonon Properties

The phonon dispersion (Figure 6.6) displays a number of regions with flat branches, most significantly around 10 THz, where there are a number of tall peaks generated in the density of states. As seen in the element-resolved phonon DOS (Figure 6.7), the lower

frequency of these peaks correspond to Al-related phonon modes, at a similar frequency to those found in MgB_2 for Mg-related modes. In contrast, $LiAlB_4$ also has a very tall peak, contributing strongly to the phonon DOS at around 10.5 THz, relating to Li-related phonon modes. This frequency relates to the three phonon modes associated with the translation of the Li layers along each of the three axes. These couple with the B and Al layers to give rise to vibrations in each layer, including two modes associated with in-plane vibrations of the B sheets. Therefore, these lower frequency and dense branches have a great deal of potential for electron-phonon coupling. Opposing this, the high-frequency B-related modes in MgB_2 have been shifted to higher frequencies, which would in turn reduce those contributions to λ. Modes at 19 THz, 22.5 THz, and 25 THz are associated with the in-plane vibrations of B atoms, expected to provide strong coupling similarly to the E_{2g} mode in MgB_2.

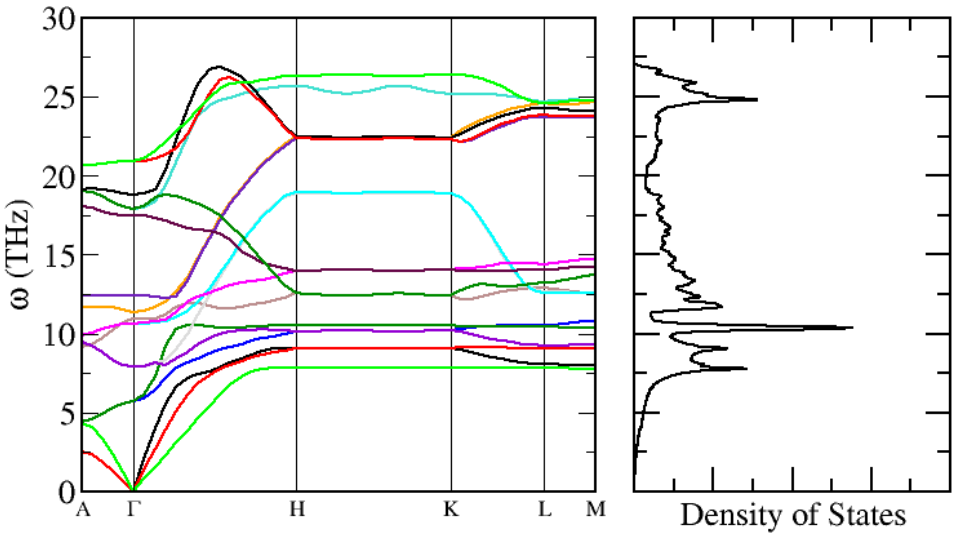

Figure 6.6: A dispersion (left) and DOS (right) plot for $LiAl_4$. The lattice points on the x-axis were used as interpolation points for the dispersion plot, while a $54 \times 54 \times 24$ fine q-point grid (offset to include the Γ-point) was used for the DOS plot.

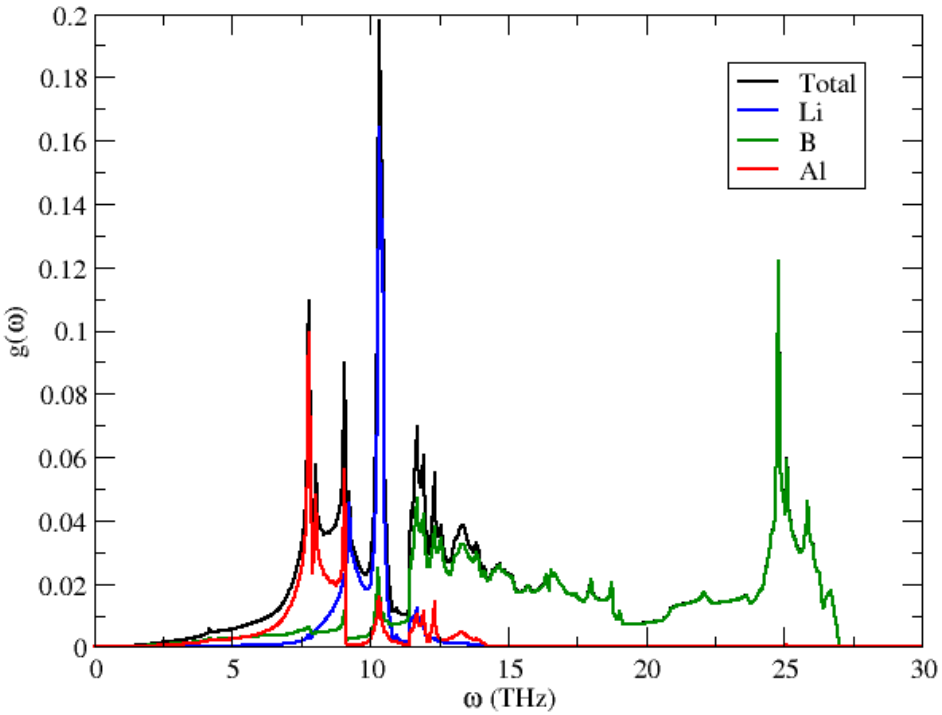

Figure 6.7: An element-resolved phonon DOS for $LiAlB_4$. It can be seen that lower frequency phonon modes are related to vibrations predominantly involving Li and Al atoms, while higher frequency modes are purely associated with B atoms.

6.3.4 Electron-Phonon Coupling and Superconductivity

Following from the discussion on vibrational properties, the Eliashberg spectral function (Figure 6.8) demonstrates that the two most significant peaks are given by phonons around 25 THz and 10.5 THz. The first of these is associated with the high-frequency, in-plane B vibrations, similar to the strong-coupling E_{2g} phonon mode which accounts for a considerable contribution to the T_c for MgB_2. Here, we also find that $LiAlB_4$ has significant λ contributions due to the vibrations (10.5 THz) arising from Li layer. This low-frequency contribution is lacking in MgB_2, for which the Mg-related modes have low coupling. These translational Li vibrations cause vibrations in both the Al and B layers as well. As such, a similar effect to the E_{2g} phonon mode may take place in which the σ-band network concentrated along the B-B axes becomes distorted, giving strong electron-phonon coupling. At a lower frequency, this also generates a stronger contribution to λ, which takes the integral of $\alpha^2F(\omega)$ divided by the phonon frequency (see Eq. (3.21)). A sum of the contributions for $LiAlB_4$ gives $\lambda = 1.104$. Taking $\mu^* = 0.1$ as we did for MgB_2, we predict for $LiAlB_4$ that $T_c = 49.39$ K with a calculated logarithmically averaged phonon frequency of 614.4 K.

Material	$N(E_f)$	ω_{log} (K)	λ	T_c (K)
MgB_2	0.7041	552.9	1.011	39.16
$LiAlB_4$	0.665*	614.4	1.104	49.39

Table 6.4: An overview of the contributing factors to the critical temperatures of MgB_2 and $LiAlB_4$. Note that $N(E_f)$ for $LiAlB_4$ is calculated for half of its unit cell, containing the same number of ions as the MgB_2 unit cell.

While $LiAlB_4$ demonstrates a low frequency, strong-coupling phonon to bolster the electron-phonon coupling constant, the hardening shift in the B-related phonon modes leads to a greater ω_{log}, representing a higher average vibrational energy. As a prefactor in the Allen-Dynes equation, this increases the T_c considerably when compared to MgB_2, which has a similar value for λ here. This corroborates the Fröhlich model predictions which demonstrates that T_c is inversely proportional to the square root of the mass. The introduction of Li ($A_r = 7$) into the system to replace Mg ($A_r = 24$) ions provides a considerable decrease in mass, even when averaged with Al ($A_r = 27$). This serves to outweigh the small reduction in $N(E_f)$ from MgB_2 to $LiAlB_4$, giving a greater critical temperature despite similar strengths in electron-phonon coupling.

Nevertheless, due to the large uncertainty in μ^* at present, using the usual range for μ^* gives an equally large uncertainty in T_c, where at the limit of the normal range for μ^* we would find a 24.7% decrease for the T_c to 37.21 K. Regardless, the predicted T_c would still be considerably high for a BCS-type superconductor and is comparable to that of MgB_2.

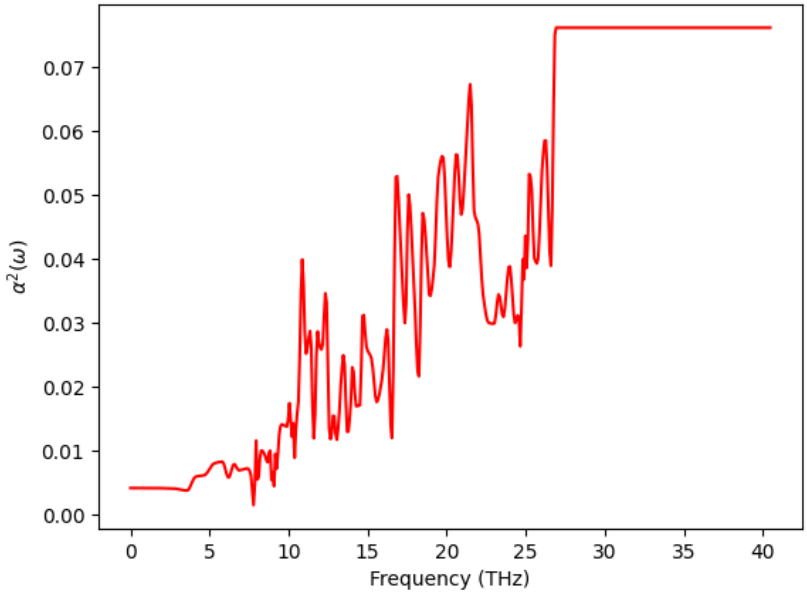

(a) $\alpha^2(\omega)$ function against phonon frequency, ω.

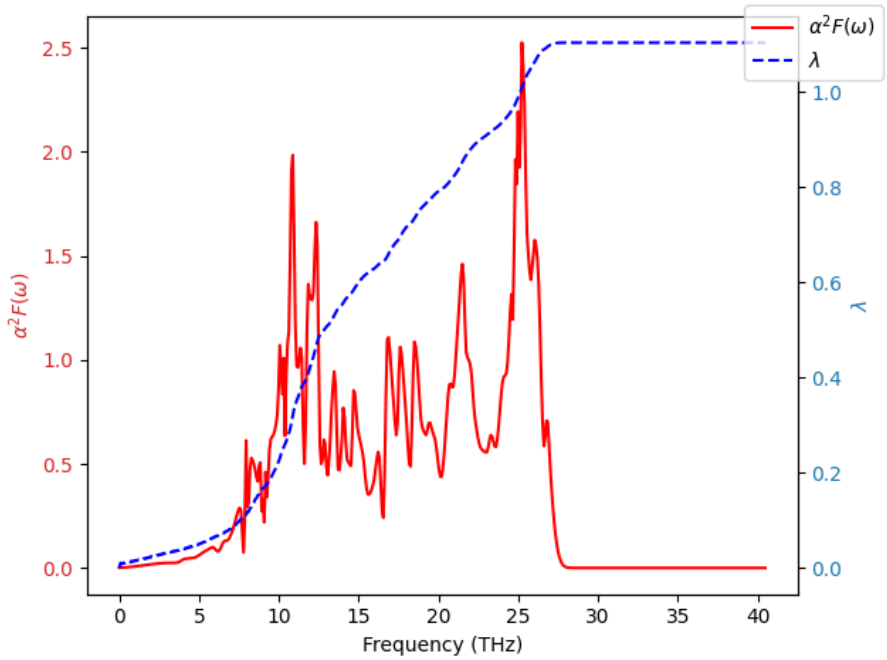

(b) $\alpha^2F(\omega)$ function (red) and the electron-phonon coupling constant λ (blue) as a cumulative sum against phonon frequency, ω.

Figure 6.8: (a) The electron-phonon coupling function and (b) the Eliashberg spectral function for $LiAlB_4$, indicating the contributions of phonon modes to superconductivity induced by electron-phonon interactions.

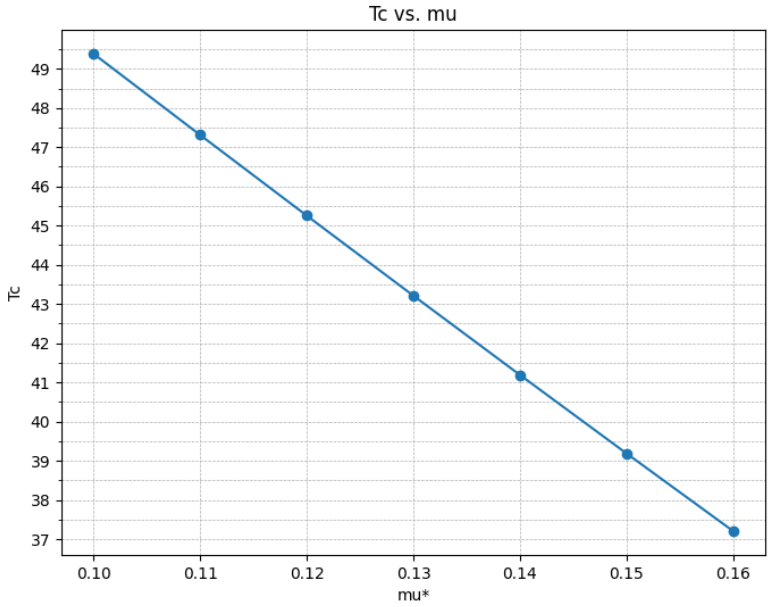

Figure 6.9: The change in T_c depending on the choice of μ^* for $LiAlB_4$.

6.4 Global Energy-Minimisation by Genetic Algorithm

Given the high T_c found for $LiAlB_4$, further testing within the condensed matter group at University of York was carried out by Scott Donaldson. Using the CASTEP genetic algorithm (GA)[86], a search for a globally energy-minimised structure for $LiAlB_4$ with a large throughput of geometry optimisations was carried out. An initial set of crystal structures for a given formula are first suggested, known as 'parent' structures. These structures are 'bred' together to produce new structures ('children'), which inherit features from the 'parent' structures. A number of 'children' are selected through a 'fitness function' based on their calculated optimised enthalpy to be used as the 'parents' for the next 'generation' of structures. Over a series of generations for variable stoichiometries, this can converge to produce a convex hull with which to predict a globally energy-minimised structure. Limitations to this include the computational cost associated with sampling a wide range of ratios of elemental species within the material and the coarse parameters used to carry out the high volume of calculations within a reasonable time-frame. Here, GA calculations have been performed across $LiAlB_4$, Li_2AlB_6, $LiAl_2B_6$, and $LiAlB_x$ ($x \in \mathbb{Z}; 2 \leq x \leq 6$).

A convex hull plot using coarse parameters (Figure 6.10) was formed using converged GA searches for these stoichiometries to compare stablities between them. The plot uses binding enthalpies (E_B) calculated through

$$E_B(Li_lAl_mB_n) = \frac{E_T(Li_lAl_mB_n) - l\mu_{Li} - m\mu_{Al} - n\mu_B}{l+n+m}, \tag{6.3}$$

where E_T is the total calculated enthalpy of a particular cell of $Li_lAl_mB_n$. μ is the chemical potential of a given species, found through the ground state structure of the element and divided by the number of ions in that unit cell. Dividing by the total number of ions provides normalisation for the cell size.

Along the convex hull, we find structures with the same layered structure as we have studied in previous sections. We will henceforth refer to the previously studied structure as α-$LiAlB_4$ for clarity. The structure found through GA convergence of the $LiAlB_4$ stoichiometry, β-$LiAlB_4$, consists of mixed metal layers rather than pure layers of Li and Al. Following a geometry optimisation with the same converged parameters used for α-$LiAlB_4$, we find an enthalpy difference of -5.84×10^{-4} eV/atom when compared to α-$LiAlB_4$. As such, a precise growth method for $LiAlB_4$ crystals may be difficult, potentially giving rise to amorphous layers or a mixture of both the α and β structures. This β-$LiAlB_4$ structure sits above the hull by approximately 0.005 eV/ion, within the error margin of the DFT calculations used. Furthermore, it is also within the room temperature

k_BT and so is still a viable structure regardless.

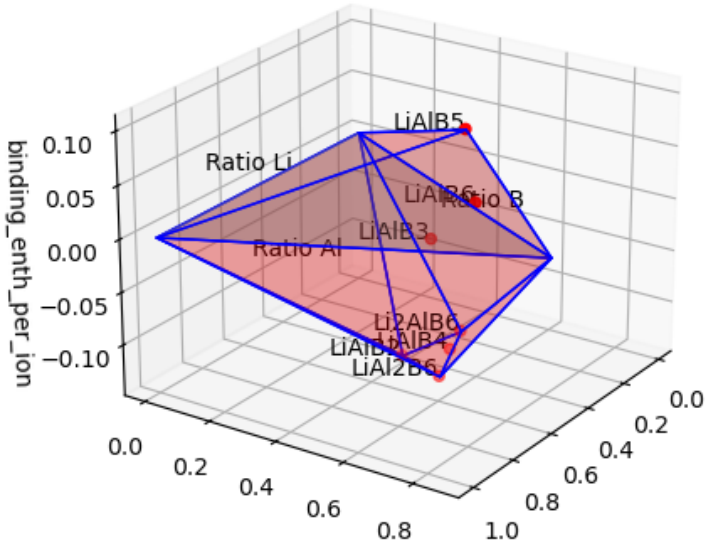

(a) A coarse convex hull plot displaying all binding enthalpies of Li-Al-B structures.

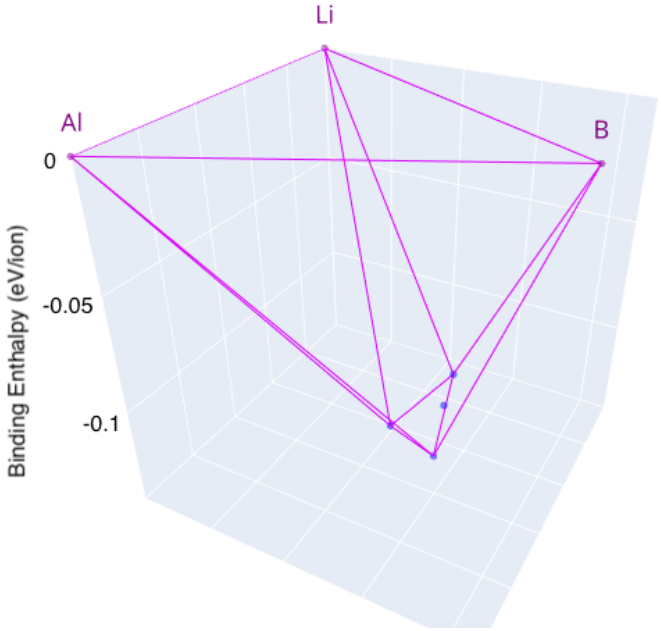

(b) A coarse convex hull plot displaying the most stable binding enthalpies of Li-Al-B structures (only negative binding enthalpies).

Figure 6.10: Approximated convex hull plots for a small number of Li-Al-B structures, made by Scott Donaldson.

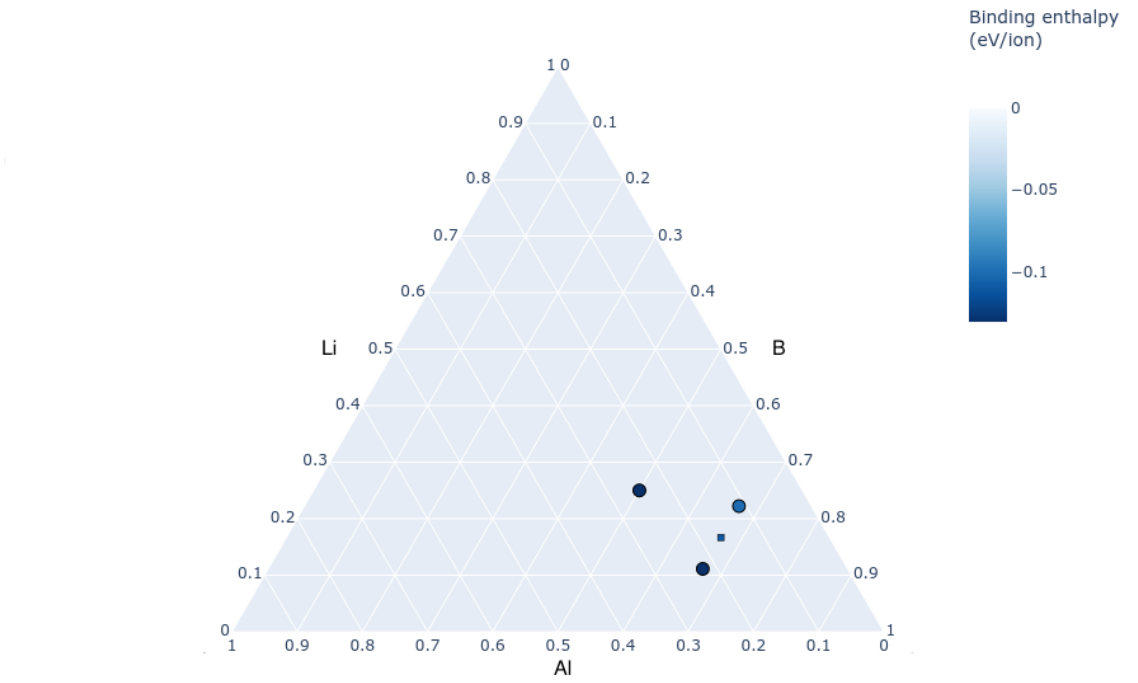

Figure 6.11: A ternary plot of the Li-Al-B made by Scott Donaldson. The small square shows the position of the β-$LiAlB_4$ structure on the plot.

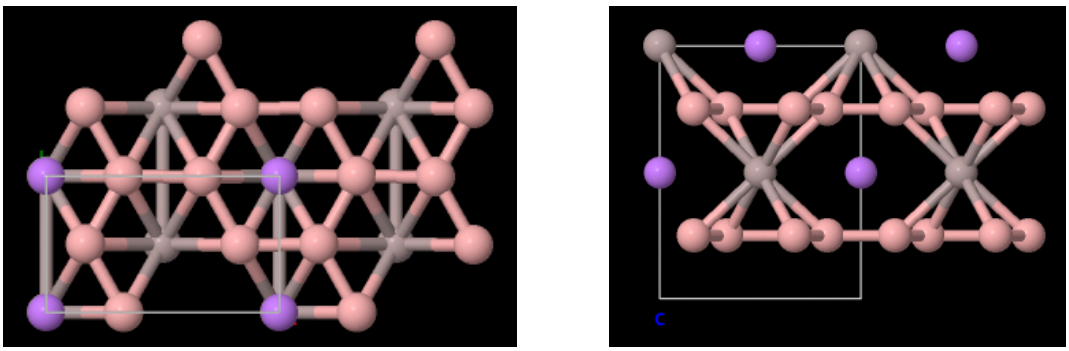

(a) β-$LiAlB_4$ as seen through the *c* axis.

(b) β-$LiAlB_4$ as seen through the *ab* plane.

Figure 6.12: The relaxed structure of the converged GA structure for $LiAlB_4$ (β-$LiAlB_4$) following a geometry optimisation. The structure consists of alternating layers of B (pink) and mixed Li (purple) and Al (grey).

Following Donaldson's work, a DOS calculation was performed for the same number of ions as the α structure unit cell, finding that the β structure has $N(E_f) = 1.24$, a 6.7% decrease from the α structure. Consequently, we can use the Fröhlich model to predict $T_c = 46.07$ K for the β structure, assuming all other factors (such as phonon modes) were equivalent. It can be expected, that on the whole, the vibrational properties should remain relatively consistent, though the effect of mixing the metal layers on the Li-related phonon

modes is currently unknown. Still, the B-related modes should persist in contributing strongly to λ.

By altering the ratios of Li and Al within the mixed metal sheets of β-$LiAlB_4$, we look at Li_2AlB_6 and $LiAl_2B_6$. As seen in Figure 6.10, these structures lie along the hull, indicating their stability with respect to other tested structures. However, altering the number of B ions in the cell generally gives a positive binding enthalpy (indicating relative instability), with the exception of the $LiAlB_2$ structures. Along with the β-$LiAlB_4$ structure, further research should be carried out on these three structures.

6.5 Conclusions

α-$LiAlB_4$ has been shown to be thermodynamically stable with respect to its constituent elements. It also proves to be dynamically stable, with a successful phonon calculation devoid of any imaginary modes. Though the density of states at the Fermi energy is lower than that of MgB_2 per unit cell, the contributions of phonons to the superconducting properties of α-$LiAlB_4$ overcome this. With in-plane B-related modes at 25 THz akin to the MgB_2 E_{2g} mode, as well as modes low-frequency modes at 10.5 THz primarily associated with Li vibrations, α-$LiAlB_4$ demonstrates stronger electron-phonon coupling than MgB_2, contributing significantly to the predicted T_c at 49.39 K. Such a result exceeds that of the MgB_2 T_c by 26%, which currently has the highest experimental T_c among BCS-type superconductors at ambient pressure. This result could be exceeded by using p-type doping to lower the Fermi level and increase $N(E_f)$.

Still, limitations within the study must be acknowledged, with the largest uncertainty remaining to be the value of μ^*, which, within its acceptable range, could lead to a decrease of 24.7% in the T_c. Outside of this, the choice of XC functional presents a common source of error for DFT calculations as this cannot exactly represent the full Schrödinger picture, though the accuracy for the MgB_2 calculations suggest that the model functions well. Finally, there is uncertainty in what structure would be found when synthesising the material for experimental works. Given the proximity of enthalpy with the β-structure, α-$LiAlB_4$ could feasibly be produced under specific growth conditions, though the possibility of an α-β mixture or the presence of amorphous layers cannot yet be discounted. Furthermore, structures such as Li_2AlB_4 and $LiAl_2B_4$ are shown to be thermodynamically viable to synthesise and could create further uncertainty in the structure of the metal layers, with a possibility of varying ratios of Li and Al. Computational limitations mean that this convex hull search is extremely coarse and, therefore, a more thorough search would be necessary to provide an accurate and full convex hull.

Chapter 7

Conclusions

The aim of this work was to apply methods for calculating the superconducting transition temperatures for materials from first principles. In Chapters 2 and 3, the theoretical frameworks with which this could be achieved were outlined before summarising the computational method within Chapter 4. It was demonstrated that early indicators to a transition temperature were given by the density of states at the Fermi energy and by phonon modes coupling strongly to electrons, notably the E_{2g} phonon mode in MgB_2 involving the vibrations of B atoms in the plane of the B sheets. Contributions from the electron-phonon coupling strength, λ, are most significant when the phonons are also at a low frequency.

In Chapter 5, MgB_2 was studied with this method, including its electronic and vibrational properties, to find a superconducting transition temperature consistent with experimental results at 39.16 K. The structural properties found were generally in agreement to other studies using a PBE functional as well as experimental data, with a highly accurate interlayer separation. The in-plane lattice parameters were also in good agreement, with a 0.4% decrease from the literature value. As discussed in Chapter 1, compressions in the *ab* plane generally lead to a reduction in the T_c, however, such a small change is unlikely to cause a significant deviation. Furthermore, the understood phonon contributions, namely with regards to the E_{2g} phonon modes, were reproduced accurately. Alongside this, contributions to $N(E_f)$ were shown to primarily come from the B p-orbitals, with $N(E_f) = 0.7041$ per unit cell. The electron-phonon coupling strength was calculated as $\lambda = 1.011$, agreeing with recent studies and correlating well with the σ-sheet coupling. The value for μ^* chosen was 0.1, at the lower end of the acceptable range of values.

In Chapter 6, a group of compounds, $XAlB_4$ (X = Li, Ca, Na, Be), are introduced.

These layered compounds are analogous to $MgAlB_4$ in that they consist of alternating layers of metal elements and boron sheets as MgB_2 does, but each metal layer alternates between pure Al or pure X. It was found that the Li-incorporated compound was most stable in this configuration, while $CaAlB_4$ had greater stability in a $YCrB_4$-type structure and Na- and Be-incorporated aluminium tetraborates were thermodynamically unstable with respect to their constituent elements. While $BeAlB_4$ was within 0.015 eV/atom, from the formation enthalpy, it was shown to also be dynamically unstable. This focused the study on $LiAlB_4$ for the remainder of the chapter.

A Mulliken charge analysis demonstrated a similar ionic nature to MgB_2 between the B and metal layers within $LiAlB_4$. The DOS calculations find $N(E_f) = 1.33$ per unit cell, which, when considered per ion, is a 5.6% decrease compared to the $N(E_f)$ for MgB_2. While also sharing similar vibrational properties, with the presence of high-frequency, in-plane B-related modes, $LiAlB_4$ has a greater phonon DOS at lower frequency, largely due to the presence of Li-related translational phonon modes which couple to the in-plane movement of B atoms for two of three axes. Both sets of phonon modes were shown to contribute significantly to the overall electron-phonon coupling strength at $\lambda = 1.104$, a 9.2% increase from MgB_2. Using $\mu^* = 0.1$ as a likely value given the structural analogue to MgB_2, we find $T_c = 49.36$ K.

While $LiAlB_4$ may indeed be a major improvement in T_c over MgB_2 as an ambient-pressure, BCS-type superconductor, the uncertainty in μ^* requires further testing through computational and, ultimately, experimental means to verify these results. Furthermore, through genetic algorithm calculations it has since become apparent that growth conditions for the material may require a high degree of precision, given that an alternate structure (β-$LiAlB_4$) in which the metal layers consist of mixed Li and Al resides at an enthalpy of -5.84×10^{-4} eV/atom below the studied structure (α-$LiAlB_4$). The ratio of Li and Al atoms in the metal layers may also be adjusted and, with a stronger Li presence, this may benefit the phonon DOS to provide greater coupling and a greater T_c in Li_2AlB_6.

As such, it has been recommended for following works to further investigate the alternative configurations suggested in Chapter 6, including but not limited to β-$LiAlB_4$, Li_2AlB_6, and $LiAl_2B_6$. Further work should include carry out phonon calculations as a means of testing the dynamic stability of each, while also providing insights to the ramifications of the mixed layers on the Li-related phonon modes. Since the completion of this research, work has been carried out by Ertugrul Karaca using Quantum Espresso to verify results and predict a T_c for the suggested structures. The T_c calculated for $LiAlB_4$ was found to be in good agreement with the results in this work. Following this, routes of synthesis should be investigated, with an aim to deduce whether or not pure α-$LiAlB_4$

synthesis is feasible, or if a mixture of the α and β structures is likely. Further testing on α-$LiAlB_4$ is advised to understand its tensile properties in greater depth (such as calculations of elastic constants) for applications in wires. To validate current results, more detailed studies should aim to converge the number of q-vectors chosen for the electron-phonon coupling calculation for greater reliability.

Bibliography

[1] Jun Nagamatsu, Norimasa Nakagawa, Takahiro Muranaka, Yuji Zenitani, and Jun Akimitsu. Superconductivity at 39 K in magnesium diboride. Nature, 410:63, 3 2001.

[2] William J. Mercer and Yuri A. Pashkin. Superconductivity: the path of least resistance to the future. Contemporary Physics, 64(1):19–46, 2023.

[3] J. Bardeen, L. N. Cooper, and J. R. Schrieffer. Theory of superconductivity. Physical Review, 108:1175–1204, 12 1957.

[4] M. L. Cohen and S. G. Louie. Fundamentals of Condensed Matter Physics. Cambridge University Press, 2016.

[5] Paul Canfield and George Crabtree. Magnesium diboride: Better late than never. Physics Today, 56:34–41, 03 2003.

[6] Sujoy Ghosh. Effect of Microstructure and Rare Earth Doping on Superconducting Properties of MgB_2 Bulk Processed by Spark Plasma Sintering. PhD thesis, University of California, 12 2021.

[7] I. I. Mazin and V. P. Antropov. Electronic structure, electron-phonon coupling, and multiband effects in MgB_2. Physica C: Superconductivity and its Applications, 385:49–65, 3 2003.

[8] Mehran Rafieazad, Özge Balcı, Selçuk Acar, and Mehmet Somer. Review on magnesium diboride (MgB_2) as excellent superconductor: Effects of the production techniques on the superconducting properties. Journal of Boron, 2:87–96, 09 2017.

[9] Hyoung Joon Choi, David Roundy, Hong Sun, Marvin L. Cohen, and Steven G. Louie. The origin of the anomalous superconducting properties of MgB_2. Nature, 418(6899):758–760, Aug 2002.

[10] Jose A. Alarco, Alison Chou, Peter C. Talbot, and Ian D. R. Mackinnon. Phonon modes of MgB2: super-lattice structures and spectral response. Phys. Chem. Chem. Phys., 16:24443–24456, 2014.

[11] Ze Yu, Tao Bo, Bo Liu, Zhendong Fu, Huan Wang, Sheng Xu, Tianlong Xia, Shiliang Li, Sheng Meng, and Miao Liu. Superconductive materials with MgB_2-like structures from data-driven screening. Physical Review B, 105, 2 2022.

[12] Elijah Lator. Superconductivity in layered transition metal (di)chalcogenides: Iron selenide and niobium diselenide. Doctoral thesis, UCL (University College London)., 10 2019.

[13] Takao Mori. Investigation of superconductivity in isoelectronic and related compounds of MgB_2. http://dx.doi.org/10.1143/JPSJS.71S.323, 71:323–325, 11 2013.

[14] Hyoung Joon Choi, Steven G. Louie, and Marvin L. Cohen. Prediction of superconducting properties of CaB_2 using anisotropic eliashberg theory. Physical Review B - Condensed Matter and Materials Physics, 80:064503, 8 2009.

[15] Dongmei Zhang, Lei Feng, Ruzheng Wang, and Yanxia Shang. A new superconductor of BeB_2C under atmospheric pressure. Journal of Superconductivity and Novel Magnetism, 35:3135–3139, 11 2022.

[16] Peng Jen Chen and Horng Tay Jeng. Ambient-pressure high-temperature superconductivity in stoichiometric hydrogen-free covalent compound $BSiC_2$. New Journal of Physics, 22:033046, 3 2020.

[17] B. A. Glowacki, M. Majoros, M. E. Vickers, and B. Zeimetz. Superconducting properties of the powder-in-tube Cu–Mg–B and Ag–Mg–B wires. Physica C: Superconductivity, 372-376:1254–1257, 8 2002.

[18] B. A. Glowacki, M. Majoros, M. Vickers, M. Eisterer, S. Toenies, H. W. Weber, M. Fukutomi, K. Komori, and K. Togano. Composite Cu/Fe/MgB_2 superconducting wires and MgB_2/YSZ/Hastelloy coated conductors for ac and dc applications. Superconductor Science and Technology, 16:297, 1 2003.

[19] M. Majoros, B. A. Glowacki, and M. E. Vickers. 50 K anomalies in superconducting MgB_2 wires in copper and silver tubes. Superconductor Science and Technology, 15:269, 1 2002.

[20] Yinchang Zhao, Zhenhong Dai, and Chao Zhang. Electronic structures and electron-phonon superconductivity of Nb_2C-based MXenes. J. Phys. D: Appl. Phys, 53:485301, 2020.

[21] Zeleke Deressa Gerbi and Pooran Singh. Effect of hydrostatic pressure on superconductivity of MgB_2. AIP Advances, 9:095038, 9 2019.

[22] Serena Margadonna, Kosmas Prassides, Ioannis Arvanitidis, Michael Pissas, Georgios Papavassiliou, and Andrew N. Fitch. Crystal structure of the $Mg_{1-x}Al_xB_2$ superconductors near $x \approx 0.5$. Phys. Rev. B, 66:014518, Jul 2002.

[23] Erik Johansson, Ferenc Tasnádi, Annop Ektarawong, Johanna Rosen, and Björn Alling. The effect of strain and pressure on the electron-phonon coupling and superconductivity in MgB_2—benchmark of theoretical methodologies and outlook for nanostructure design. Journal of Applied Physics, 131:063902, 2 2022.

[24] A. Serquis, Y. T. Zhu, E. J. Peterson, J. Y. Coulter, D. E. Peterson, and F. M. Mueller. Effect of lattice strain and defects on the superconductivity of MgB_2. Applied Physics Letters, 79:4399, 12 2001.

[25] Zhao Liu and Biao Wang. Biaxial strain engineering on the superconducting properties of MgB_2 monolayer. Materials Chemistry and Physics, 290:126637, 2022.

[26] Akira Yamamoto. Advances in MgB_2 superconductor applications for particle accelerators. Journal reference: TEION KOGAKU (J. CSSJ), 57:17–22, 2022.

[27] B. Savaskan, U.K. Ozturk, S.B. Guner, M. Abdioglu, M.V. Bahadır, S. Acar, M. Somer, A.M. Ionescu, C. Locovei, M. Enculescu, and P. Badica. Bulk MgB_2 superconductor for levitation applications fabricated with boron processed by different routes. Journal of Alloys and Compounds, 961:170893, 2023.

[28] Dipak Patel, Akiyoshi Matsumoto, Hiroaki Kumakura, Minoru Maeda, Sun-Hu Kim, Hao Liang, Yusuke Yamauchi, Seyong Choi, Jung Ho Kim, and Md. Shahriar A. Hossain. Superconducting joints using multifilament MgB_2 wires for MRI application. Scripta Materialia, 204:114156, 2021.

[29] A. Ballarino and R. Flükiger. Status of MgB_2 wire and cable applications in Europe. Journal of Physics: Conference Series, 871(1):012098, jul 2017.

[30] Elias Galan, Thomas Melbourne, Bruce Davidson, X. Xi, and Ke Chen. Multilayer MgB_2 superconducting quantum interference filter magnetometers. Applied Physics Letters, 108:172602, 04 2016.

[31] L Lolli, T Li, C Portesi, E Taralli, N Acharya, K Chen, M Rajteri, D Cox, E Monticone, J Gallop, and L Hao. Micro-SQUIDs based on MgB_2 nano-bridges for NEMS readout. Superconductor Science and Technology, 29(10):104008, sep 2016.

[32] S. J. Clark, M. D. Segall, C. J. Pickard, P. J. Hasnip, M. J. Probert, K. Refson, and M.C. Payne. First principles methods using CASTEP. Z. Kristall., 220:567–570, 2005.

[33] Paul Adrien Maurice Dirac and Ralph Howard Fowler. Quantum mechanics of many-electron systems. Proceedings of the Royal Society of London. Series A, Containing Papers of a Mathematical and Physical Character, 123:714–733, 1929.

[34] Bhupalee Kalita, Li Li, Ryan McCarty, and Kieron Burke. Learning to approximate density functionals. Accounts of chemical research, 54, 02 2021.

[35] Ivana Paidarová and Stephan P. A. Sauer. A comparison of density functional theory and coupled cluster methods for the calculation of electric dipole polarizability gradients of methane. AIP Conference Proceedings, 1504:695–698, 01 2012.

[36] M. Born and R. Oppenheimer. Zur quantentheorie der molekeln. Annalen der Physik, 389(20):457–484, 1927.

[37] Peter J. P. Byrne. An Ab-Initio Study of the properties of Superconductors under Perturbations. PhD thesis, University of Durham, 2017.

[38] J. I. Steinfeld. Molecules and Radiation: An Introduction to Modern Molecular Spectroscopy. MIT Press, Cambridge, 1985.

[39] Peter D. Haynes. Linear-scaling methods in ab initio quantum-mechanical calculations. PhD thesis, University of Cambridge, 1998.

[40] P. Hohenberg and W. Kohn. Inhomogeneous electron gas. Phys. Rev., 136:B864–B871, Nov 1964.

[41] W. Kohn and L. J. Sham. Self-consistent equations including exchange and correlation effects. Phys. Rev., 140:A1133–A1138, Nov 1965.

[42] Douglas Hartree. The wave mechanics of an atom with a non-coulomb central field. Mathematical Proceedings of the Cambridge Philosophical Society, 24, 1928.

[43] Vladimir Fock. Näherungsmethode zur lösung des quantenmechanischen mehrkörperproblems. Zeitschrift für Physik, 61, 1930.

[44] John C. Slater. Quantum theory of many-electron systems and its application to the structure of atoms. Physical Review, 36(1), 1930.

[45] Kieron Burke. Perspective on density functional theory. The Journal of Chemical Physics, 136(15):150901, 04 2012.

[46] A. D. Becke. Density-functional exchange-energy approximation with correct asymptotic behavior. Phys. Rev. A, 38:3098–3100, Sep 1988.

[47] John P. Perdew and Yue Wang. Accurate and simple analytic representation of the electron-gas correlation energy. Phys. Rev. B, 45:13244–13249, Jun 1992.

[48] Yingkai Zhang and Weitao Yang. Comment on "Generalized gradient approximation made simple". Phys. Rev. Lett., 80:890–890, Jan 1998.

[49] Axel D. Becke. Density-functional thermochemistry. IV. A new dynamical correlation functional and implications for exact-exchange mixing. The Journal of Chemical Physics, 104(3):1040–1046, 01 1996.

[50] John P. Perdew, Kieron Burke, and Matthias Ernzerhof. Generalized gradient approximation made simple. Phys. Rev. Lett., 77:3865–3868, Oct 1996.

[51] Viktor N. Staroverov, Gustavo E. Scuseria, Jianmin Tao, and John P. Perdew. Tests of a ladder of density functionals for bulk solids and surfaces. Phys. Rev. B, 69:075102, Feb 2004.

[52] L. P. Bouckaert, R. Smoluchowski, and E. Wigner. Theory of brillouin zones and symmetry properties of wave functions in crystals. Phys. Rev., 50:58–67, Jul 1936.

[53] I J Robertson and M C Payne. k-point sampling and the k.p method in pseudopotential total energy calculations. Journal of Physics: Condensed Matter, 2(49):9837, dec 1990.

[54] Phil Hasnip. Pseudopotentials, 2021. URL `https://www-users.york.ac.uk/~mijp1/teaching/grad_FPMM/lecture_notes/lec11_pseudopotentials.pdf`. Accessed on 5th Feb 2024.

[55] D. R. Hamann, M. Schlüter, and C. Chiang. Norm-conserving pseudopotentials. Phys. Rev. Lett., 43:1494–1497, Nov 1979.

[56] David Vanderbilt. Soft self-consistent pseudopotentials in a generalized eigenvalue formalism. Phys. Rev. B, 41:7892–7895, Apr 1990.

[57] R. P. Feynman. Forces in molecules. Phys. Rev., 56:340–343, Aug 1939.

[58] János Ángyán. Wigner's (2n + 1) rule for nonlinear Schrödinger equations. Journal of Mathematical Chemistry, 46:1–14, 06 2009.

[59] Stefano Baroni, Paolo Giannozzi, and Andrea Testa. Green's-function approach to linear response in solids. Phys. Rev. Lett., 58:1861–1864, May 1987.

[60] Rolf Heid. The Physics of Correlated Insulators, Metals, and Superconductors. Institute for Advanced Simulation, 08 2017.

[61] W. L. McMillan. Transition temperature of strong-coupled superconductors. Phys. Rev., 167:331–344, Mar 1968.

[62] Feliciano Giustino. Electron-phonon interactions from first principles. Reviews of Modern Physics, 89:015003, 2 2017.

[63] P. B. Allen and R. C. Dynes. Transition temperature of strong-coupled superconductors reanalyzed. Phys. Rev. B, 12:905–922, Aug 1975.

[64] E Karaca, P J P Byrne, P J Hasnip, H M Tütüncü, and M I J Probert. Electron–phonon interaction and superconductivity in hexagonal ternary carbides Nb_2AC (A: Al, S, Ge, As and Sn). Electronic Structure, 3(4):045001, oct 2021.

[65] E. Karaca, P. J. P. Byrne, P. J. Hasnip, and M. I. J. Probert. Cr_2AlN and the search for the highest temperature superconductor in the M_2AX family. Scientific Reports, 13(1):6576, Apr 2023.

[66] Richard P. Feynman. Simulating physics with computers. International Journal of Theoretical Physics, 21:467–488, 6 1982.

[67] Andrew J. Morris, Rebecca J. Nicholls, Chris J. Pickard, and Jonathan R. Yates. Optados: A tool for obtaining density of states, core-level and optical spectra from electronic structure codes. Computer Physics Communications, 185(5):1477–1485, 2014.

[68] M. C. Payne, M. P. Teter, D. C. Allan, T.A. Arias, and J. D. Joannopoulos. Iterative minimization techniques for ab initio total-energy calculations - molecular-dynamics and conjugate gradients. Rev. Mod. Phys., 64:1045–1097, 1992.

[69] Matt Probert. Reciprocal space description of electrons and phonon states, 2021. URL `https://www-users.york.ac.uk/~mijp1/teaching/grad_FPMM/lecture_notes/lec3_reciprocal_space.pdf`. Accessed on 15th Feb 2024.

[70] Xavier Gonze and Changyol Lee. Dynamical matrices, born effective charges, dielectric permittivity tensors, and interatomic force constants from density-functional perturbation theory. Phys. Rev. B, 55:10355–10368, Apr 1997.

[71] Sergey Lee, Hatsumi Mori, Takahiko Masui, Yuri Eltsev, Ayako Yamamoto, and Setsuko Tajima. Growth, structure analysis and anisotropic superconducting properties of MgB_2 single crystals. Journal of the Physical Society of Japan, 70(8):2255–2258, 2001.

[72] Andrew J. Morris, Rebecca J. Nicholls, Chris J. Pickard, and Jonathan R. Yates. Optados: A tool for obtaining density of states, core-level and optical spectra from electronic structure codes. Computer Physics Communications, 185(5):1477–1485, May 2014.

[73] Rebecca Nicholls, A Morris, C Pickard, and J Yates. Optados - a new tool for eels calculations. Journal of Physics: Conference Series, 371, 07 2012.

[74] Jonathan R. Yates, Xinjie Wang, David Vanderbilt, and Ivo Souza. Spectral and fermi surface properties from wannier interpolation. Phys. Rev. B, 75:195121, May 2007.

[75] Pablo de la Mora, Miguel Castro, and Gustavo Tavizon. Comparative study of the electronic structure of alkaline-earth borides (MeB_2; Me=Mg, Al, Zr, Nb, and Ta) and their normal-state conductivity. Journal of Solid State Chemistry, 169(2):168–175, 2002.

[76] Alexandre Tkatchenko and Matthias Scheffler. Accurate molecular van der waals interactions from ground-state electron density and free-atom reference data. Phys. Rev. Lett., 102:073005, Feb 2009.

[77] J. D. Jorgensen, D. G. Hinks, and S. Short. Lattice properties of MgB_2 versus temperature and pressure. Phys. Rev. B, 63:224522, May 2001.

[78] Chang-Eun Kim, Keith G. Ray, David F. Bahr, and Vincenzo Lordi. Electronic structure and surface properties of MgB_2(0001) upon oxygen adsorption. Phys. Rev. B, 97:195416, May 2018.

[79] Yoyo Hinuma, Giovanni Pizzi, Yu Kumagai, Fumiyasu Oba, and Isao Tanaka. Band structure diagram paths based on crystallography. Computational Materials Science, 128:140–184, February 2017.

[80] Atsushi Togo and Isao Tanaka. `Spglib`: a software library for crystal symmetry search, 2018.

[81] E. R. Margine and F. Giustino. Anisotropic migdal-eliashberg theory using wannier functions. Phys. Rev. B, 87:024505, Jan 2013.

[82] Truong Tho Pham and Duc Long Nguyen. First-principles prediction of superconductivity in MgB_3C_3. Physical Review B, 107:134502, 4 2023.

[83] C. Tayran, S. Aydin, M. Çakmak, and Ş. Ellialtıoğlu. Alkali and alkaline earth metal doped aluminum tetraborides containing intrinsic planar boron sheet: $XAlB_4$ (X=Li, Mg, Ca, and Na). Computational Materials Science, 124:130–141, 2016.

[84] Kuan-Rong Hao, Qing-Bo Yan, and Gang Su. Boron based layered electrode materials for metal-ion batteries. Phys. Chem. Chem. Phys., 22:709–715, 2020.

[85] A. Tampieri, G. Celotti, S. Sprio, D. Rinaldi, G. Barucca, and R. Caciuffo. Effects of copper doping in mgb2 superconductor. Solid State Communications, 121(9):497–500, 2002.

[86] N. L. Abraham and M. I. J. Probert. Improved real-space genetic algorithm for crystal structure and polymorph prediction. Phys. Rev. B, 77:134117, Apr 2008.